Towards deconvolution to enhance the grid method for in-plane strain measurement

Frédéric Sur, Michel Grediac

Towards deconvolution to enhance the grid method for in-plane strain measurement

Frédéric SUR, **Michel** GRÉDIAC

ISSN 0249-6399 ISRN INRIA/RR--8126--FR+ENG

RESEARCH REPORT
N° 8126
November 2012
Project-Team Magrit & Institut Pascal (Clermont Université)

Towards deconvolution to enhance the grid method for in-plane strain measurement

Frédéric Sur*, Michel Grédiac†

Project-Team Magrit & Institut Pascal (Clermont Université)

Research Report n° 8126 — November 2012 — 37 pages

Abstract: The grid method is one of the available techniques to measure in-plane displacement and strain components on a deformed material. A periodic grid is first transferred on the specimen surface, and then images of the grid are compared before and after deformation. Windowed Fourier analysis-based techniques then permits to estimate the in-plane displacement maps and the strain components. In this report, we give a precise analysis of this estimation process. We show that the retrieved displacement maps and strain components are actually a tight approximation of the convolution of the actual displacements and strains with the analysis window. We also characterize the effect of digital image noise on the retrieved quantities and we prove that the resulting noise can be approximated by a stationary spatially correlated noise. These results are of utmost importance to enhance the metrological performance of the grid method, as shown in a separate report [11].

Key-words: Experimental solid mechanics, grid method, windowed Fourier analysis, correlated noise.

* LORIA - projet Magrit, Université de Lorraine, CNRS, INRIA, UMR 7503. Campus Scientifique BP 239, 54506 Vandœuvre-lès-Nancy cedex, France.

† Clermont Université, Université Blaise Pascal, Institut Pascal, UMR CNRS 6602. BP 10448, 63000 Clermont-Ferrand, France

RESEARCH CENTRE
NANCY – GRAND EST

615 rue du Jardin Botanique
CS20101
54603 Villers-lès-Nancy Cedex

Vers des méthodes de déconvolution pour améliorer les performances de la méthode de la grille pour la mesure de champs de déformations planes

Résumé : La méthode de la grille est une des techniques de champs permettant de mesurer les déplacements ou les déformations à la surface d'un matériau subissant une sollicitation. Une grille périodique est transférée sur la surface de l'éprouvette considérée, et des images de la grille avant et après déformation sont comparées. Des techniques basées sur l'analyse de Fourier à fenêtre permettent alors d'estimer les cartes des composantes planes des déplacements et des déformations. Nous analysons dans ce rapport ce processus d'estimation. Nous montrons que les cartes estimées des déplacements et des déformations sont en fait bien approchées par la convolution des cartes réelles des déplacements et des déformations avec la fenêtre d'analyse. D'autre part, nous caractérisons la manière dont le bruit présent dans l'image de la grille se transfère sur les quantités estimées, et nous prouvons que le bruit résultant peut être approché par un bruit stationnaire spatialement corrélé. Ces résultats sont importants pour améliorer les performances métrologiques de la méthode de la grille, comme expliqué dans un rapport dédié [11].

Mots-clés : Mécanique des solides expérimentale, méthode de la grille, analyse de Fourier à fenêtre, bruit corrélé.

1 Introduction

One of the full-field methods available for in-plane displacement and strain measurement in experimental solid mechanics is the grid method. This technique relies on the analysis of images of a regular grid attached on the surface of a specimen to be analyzed. Typically, this specimen is subjected to a load whose amplitude is measured, yielding surface deformation. Analyzing the relationship between applied load and strain that occurs on the surface, either at the global or the local level, provides valuable information concerning the mechanical response of the constitutive material. An example can be seen in figure 1. The mechanical device through which the load is depicted in figure 1-a. The front face is illuminated by three flexible and movable light guides fed by a cold light source. They provide a regular lighting of the grid which is deposited on the front face of the specimen prior to test. Figure 1-b shows a picture of the specimen face captured by the camera. It has a nearly uniform gray color, but the zoom in figure 1-c shows that this quasi-uniform color can be seen as an average between the black and white colors of the lines that constitute the grid. In this last figure, each pixel represents a surface whose area is 40×40 micrometers^2 on the specimen, the pitch of the grid being encoded with 5 pixels. It is also worth noting that the gray level is not rigorously constant along the lines and that some local defects due to lack of paint locally occurs.

The objective here is to measure the displacement and strain fields at each pixel of the grid image. Compared to many other fields of imaging, it must be pointed out that the amplitude of the displacement due to deformation (the one due to rigid-body like movements is not discussed here) is generally very small, if not tiny since it is typically equal to some micrometers to some tens of mm. In addition, this displacement field is not uniform throughout the specimen and in the context of material and structure testing, we are interested in measuring the components of the in-plane strain tensor which is defined by the symmetric part of the displacement gradient [2]. Since we deal here with measurements and since strain components are often the sought quantities (thus spatial derivatives are to be calculated), the influence of noise on the measured quantities is a key-issue, as discussed in this report.

Compared to digital image correlation (DIC) which is another full-field measurement technique widely used in experimental solid mechanics [18], it can be said that we rely here on a regular marking of the surface instead of a random one for DIC (typically speckles.) From a practical point of view, this is a drawback because depositing a speckle is much easier than depositing a grid. On the contrary, this is a big advantage concerning image processing since we can rely here on the powerful Fourier analysis of this regular marking to deduce the displacement and strain fields from the grid images shot during the test and to analyze the metrological performance, as performed in the current report.

The grid behaves like a spatial carrier. The information in terms of displacement and strain is contained in the deviation from periodicity of this pseudo-periodic signal and its derivatives. Among various techniques available for processing this type of image [19, 16, 10, 12, 4], the most popular is based on the windowed Fourier transform (or Short Time Fourier Transform, STFT) [5, 17]. The aim of this report is to accurately analyze this estimation process, which is often used routinely. The contributions are twofold. We first prove that the deformation maps (resp. strain components) given by the windowed Fourier transform are actually well approximated by the convolution between the true deformation maps (resp. strain components), and the window function of the STFT. This is valid under assumptions which hold in the case of interest, basically because the specimen undergoes surface deformations which are very small: around some percents maximum. Many papers available in the recent literature show that this technique has been used to measure strain fields on the surface of specimens made in various types of constitutive materials.

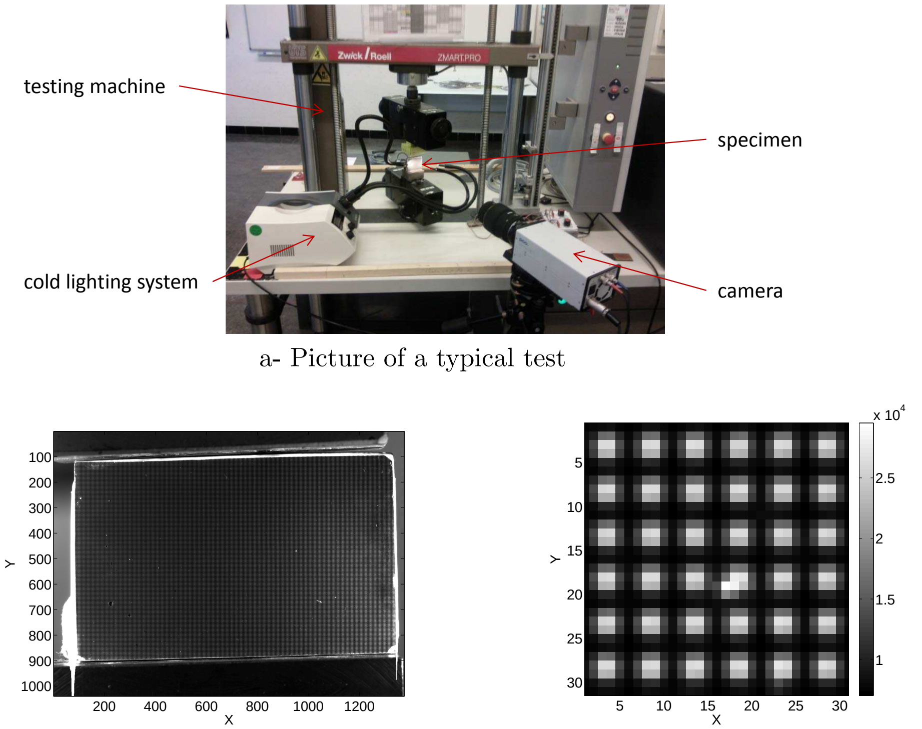

a- Picture of a typical test

b- Front view of the specimen equipped with a grid   c- Enlargement of the grid image

Figure 1: Typical test and measurements with the grid method.

We also prove that a Gaussian white noise on the digital grid image yields a stationary, spatially correlated noise on the retrieved deformation maps and strain components as well. The present theoretical study will allow us to use deconvolution techniques to get enhanced measures of strain components, which is the subject of a dedicated report [11]. Moreover, this report is also of interest for fringe pattern analysis in optical interferometry [14, 17] since the grid method can be seen as a special case in this framework.

Reader's guide. Section 2 is about the ideal, noise-free and continuous model of the grid image. In this section, we formalize the framework and make the connection between the phase of the windowed Fourier transform and the local perturbations of the grid due to the specimen deformations. Several theorems giving bounds are stated and proved in a separate subsection for the sake of reading flow. We argue that the bounds are indeed small with respect to the quantities of interest, based on the typical values of the mechanical problem. This yields useful approximations of the quantities of interest. Then, section 3 is about the noise on the grid image and its influence on the displacements and strains. The discussion is based on first order approximations. The results of this report are assessed and illustrated by numerical experiments in section 4. We conclude in section 5.

2 The ideal, noise-free and continuous model

2.1 Formalism and purpose of the study

As in [5], the light intensity of a grid image is modeled by a function $s : \mathbb{R}^2 \to \mathbb{R}$ from the image plane to the set of the gray-level values such that for every $(x, y) \in \mathbb{R}^2$:

$$s(x,y) = \frac{A}{2}\Big(2 + \gamma \cdot \mathsf{frng}(2\pi f x + \phi_1(x,y)) + \gamma \cdot \mathsf{frng}(2\pi f y + \phi_2(x,y))\Big) \tag{1}$$

where:

- A is the global field illumination;
- γ is the contrast of the oscillatory pattern, assumed constant here;
- $\mathsf{frng} : \mathbb{R} \to \mathbb{R}$ is a real 2π-periodic function with a peak-to-peak amplitude equal to 1 and average value 0;
- f is the frequency of the carrier, defined as the inverse of the pattern pitch p (that is, the inter-line distance);
- $\phi_1(x, y)$ and $\phi_2(x, y) : \mathbb{R}^2 \to \mathbb{R}$ are the carrier phase modulations along the $x-$ and $y-$axes respectively, supposed to be C^2. We will call ϕ_1 and ϕ_2 the phase maps.

Let us remark that the light intensity model slightly differs from the actual grid image in some aspects. For example at the crossing of $x-$ and $y-$ lines the gray-level is not exactly twice as high as the intensity of the lines; the contrast γ is not exactly constant along the lines; and the field illumination is uneven because of vignetting and non-uniform lightning. However, we will neglect these problems since this model proves to be accurate enough for our purposes. In particular, as we will see, we use the windowed Fourier transform. Gentle variations of γ and A across the grid image are therefore not annoying, until these quantities can be considered constant inside the analysis window.

Since the frequency f is not exactly constant because of the manufacturing process of the grid, the phase maps ϕ_1 and ϕ_2 are not zero before deformation. Once ϕ_1 and ϕ_2 are extracted from the grid image before and after deformation, it is possible to derive the in-plane displacement u_x and u_y in the x- and y-directions by forming the following phase variations:

$$\begin{cases} u_x = -\frac{p}{2\pi}\Delta\phi_1 \\ u_y = -\frac{p}{2\pi}\Delta\phi_2 \end{cases} \tag{2}$$

The linearized strain components are eventually given by the symmetrized part of the displacement gradient [2]. Thus:

$$\begin{cases} \varepsilon_{xx} = \frac{\partial u_x}{\partial x} = -\frac{p}{2\pi}\Delta\frac{\partial \phi_1}{\partial x} \\ \varepsilon_{yy} = \frac{\partial u_y}{\partial y} = -\frac{p}{2\pi}\Delta\frac{\partial \phi_2}{\partial y} \\ \varepsilon_{xy} = \frac{1}{2}\left(\frac{\partial u_x}{\partial y} + \frac{\partial u_y}{\partial x}\right) = -\frac{p}{4\pi}\left(\Delta\frac{\partial \phi_1}{\partial y} + \Delta\frac{\partial \phi_2}{\partial x}\right) \end{cases} \tag{3}$$

Hence, estimating displacements and strain components come down to retrieving the phase maps and their derivatives from a grid image. The phase modulations ϕ_1 and ϕ_2 are classically retrieved from the windowed Fourier transform [17]. More precisely, let us note for any $(\xi,\eta)\in\mathbb{R}^2$ and $\theta\in[0,2\pi)$:

$$\Psi(\xi,\eta,\theta)=\iint_{\mathbb{R}^2} s(x,y)g_\sigma(x-\xi,y-\eta)e^{-2i\pi f(x\cos(\theta)+y\sin(\theta))}\,\mathrm{d}x\,\mathrm{d}y \tag{4}$$

where g_σ is a 2D window function of width σ, symmetric, positive, and integrating to 1. We also assume that $g_\sigma(x,y)=\sigma^{-2}g(x/\sigma,y/\sigma)$ where g is some window envelope. In this case, $\iint g_\sigma=1$ as soon as $\iint g=1$.

In this report, we choose a 2D standard Gaussian function for g, i.e.

$$g(x,y)=\frac{1}{2\pi}e^{-(x^2+y^2)/2} \tag{5}$$

Nevertheless, the proofs can be adapted so that the theorems still hold for any standard window envelope (e.g. a triangle envelope.)

Remark that $\Psi(x,y,\theta)$ is nothing but the windowed Fourier transform restricted to the circle of radius f in the frequency domain. If h is any integrable 2D function, we note $\widehat{h}$ its Fourier transform: $\widehat{h}(\alpha,\beta)=\iint h(x,y)e^{-2i\pi(x\alpha+y\beta)}\,\mathrm{d}x\,\mathrm{d}y$. In particular: $\widehat{g_\sigma}(\xi,\eta)=e^{-2\pi^2\sigma^2(\xi^2+\eta^2)}$. Note that if h is symmetric with respect to 0, then also $\widehat{h}$ has this property.

Within this framework, it is classic to use the phase of the complex $\Psi(\xi,\eta,0)$ as an estimate of $\phi_1(\xi,\eta)$ and the phase of $\Psi(\xi,\eta,\pi/2)$ as an estimate of $\phi_2(\xi,\eta)$. We show that, within natural assumptions that we will precise, ϕ_1 and ϕ_2 are actually linked to Ψ via:

$$\mathrm{angle}(\Psi(\xi,\eta,0))\simeq\alpha+\iint\phi_1(x,y)g_\sigma(x-\xi,y-\eta)\,\mathrm{d}x\,\mathrm{d}y\mod(2\pi) \tag{6}$$

and:

$$\mathrm{angle}(\Psi(\xi,\eta,\pi/2))\simeq\alpha+\iint\phi_2(x,y)g_\sigma(x-\xi,y-\eta)\,\mathrm{d}x\,\mathrm{d}y\mod(2\pi) \tag{7}$$

where α is a constant depending only on the frng function, angle(z) denotes a determination in $[0,2\pi)$ of the phase of any complex number $z\neq0$, and the equality holds modulo 2π. The constant α can be omitted here. Phase maps are indeed often either differentiated or subtracted between images of the same grid taken at two different instants, the surface under investigation having deformed in between and the lighting being almost unchanged, as explained in section 2.1, eq. (2) and (3).

We also show that the approximation still holds for the ξ- and η-derivatives of the left- and right-hand terms of these equations, that is:

$$\frac{\partial}{\partial\cdot}\mathrm{angle}(\Psi(\xi,\eta,0))\simeq\iint\frac{\partial\phi_1}{\partial\cdot}(x,y)g_\sigma(x-\xi,y-\eta)\,\mathrm{d}x\,\mathrm{d}y\mod(2\pi) \tag{8}$$

$$\frac{\partial}{\partial\cdot}\mathrm{angle}(\Psi(\xi,\eta,\pi/2))\simeq\iint\frac{\partial\phi_2}{\partial\cdot}(x,y)g_\sigma(x-\xi,y-\eta)\,\mathrm{d}x\,\mathrm{d}y\mod(2\pi) \tag{9}$$

where $\cdot$ denotes either ξ or η.

Since g_σ is symmetric, this simply means that the phase of $\Psi(x,y,0)$ (resp. $\Psi(x,y,\pi/2)$) is approximately the convolution[1] of the sought phase modulation ϕ_1 (resp. ϕ_2) by the window function g_σ. The same remark holds for the derivatives.

[1] If f_1 and f_2 are two integrable functions on $\mathbb{R}^n$, their convolution product is $f_1*f_2(\mathbf{x})=\int_{\mathbb{R}^n}f_1(\mathbf{y})f_2(\mathbf{x}-\mathbf{y})\,\mathrm{d}\mathbf{y}$.

2.2 Theorems and practical approximations

In this section we derive the approximations given by equations (6) to (9) and we precise under which assumptions they hold.

2.2.1 Getting the phase from the Fourier transform on the circle

Without loss of generality, we focus now on $\Psi(\xi,\eta,0)$. The results indeed easily transfer to $\Psi(\xi,\eta,\pi/2)$. Let us note:

$$I_1(\xi,\eta) = \iint g_\sigma(x-\xi, y-\eta) e^{-i2\pi f x}\,\mathrm{d}x\,\mathrm{d}y \tag{10}$$

$$I_2(\xi,\eta) = \iint \mathsf{frng}(2\pi f x + \phi_1(x,y)) g_\sigma(x-\xi, y-\eta) e^{-i2\pi f x}\,\mathrm{d}x\,\mathrm{d}y \tag{11}$$

$$I_3(\xi,\eta) = \iint \mathsf{frng}(2\pi f y + \phi_2(x,y)) g_\sigma(x-\xi, y-\eta) e^{-i2\pi f x}\,\mathrm{d}x\,\mathrm{d}y \tag{12}$$

so that:

$$\Psi(\xi,\eta,0) = AI_1(\xi,\eta) + \frac{\gamma A}{2} I_2(\xi,\eta) + \frac{\gamma A}{2} I_3(\xi,\eta). \tag{13}$$

Since frng is a 0-mean 2π-periodic function, its Fourier series is:

$$\mathsf{frng}(x) = \sum_{k\in\mathbb{Z}} d_k e^{ikx} \tag{14}$$

where $d_0 = 0$. We also assume $d_1 \neq 0$ for the sake of reading flow. We will briefly come back to this assumption in section 3.2.4, with insights given by noise propagation.

We also note $\mathbb{Z}^*$ the set of non-zero integers, $\nabla(\phi)$ the gradient of any derivable function ϕ, $< \cdot, \cdot >$ the canonical scalar product, and $||\cdot||_2$ the Euclidean norm in $\mathbb{R}^2$. Let us also define for any C^2 function ϕ from $\mathbb{R}^2$ to $\mathbb{R}$:

$$M_\sigma(\phi)(\xi,\eta) = \frac{1}{2} \iint |(x,y)\mathcal{H}_{(x,y)}^{(\xi,\eta)}(x,y)^T| \cdot g_\sigma(x,y)\,\mathrm{d}x\,\mathrm{d}y \tag{15}$$

where $\mathcal{H}_{(x,y)}^{(\xi,\eta)}$ is a 2×2 matrix such that the Taylor series expansion (see proposition A.3 in appendix) of ϕ is:

$$\phi(x+\xi, y+\eta) = \phi(\xi,\eta) + < (x,y), \nabla\phi(\xi,\eta) > + \frac{1}{2}(x,y)\cdot H(\xi + h_1 x, \eta + h_2 y)\cdot (x,y)^T \tag{16}$$

where H is the Hessian matrix of ϕ, $h_1, h_2 \in [0,1]$, and for every $(i,j) \in \{1,2\}\times\{1,2\}$,

$$\left| \left(\mathcal{H}_{(x,y)}^{(\xi,\eta)}\right)_{i,j} \right| = \sup_{[\xi,x],[\eta,y]} |H_{i,j}| \tag{17}$$

Let us also note $D = \sum_{k\in\mathbb{Z}} |kd_k|$.

With these notations, the following theorem is proved in section 2.3.

Theorem 2.1 *The following relations hold:*

$$|I_1(\xi,\eta)| = |\widehat{g_\sigma}(f,0)| \tag{18}$$

$$|I_3(\xi,\eta)| \leq \sum_{k\in\mathbb{Z}^*} |d_k| \widehat{g_\sigma}\left(f - \frac{k}{2\pi}\frac{\partial \phi_2}{\partial \xi}(\xi,\eta), fk - \frac{k}{2\pi}\frac{\partial \phi_2}{\partial \eta}(\xi,\eta)\right) + D \cdot M_\sigma(\phi_2)(\xi,\eta) \tag{19}$$

$$I_2(\xi,\eta) = d_1 \iint g_\sigma(x-\xi, y-\eta) e^{i\phi_1(x,y)}\ dx\ dy + I_2'(\xi,\eta) \tag{20}$$

where:

$$|I_2'(\xi,\eta)| \leq \sum_{k\neq 0,1} |d_k| \widehat{g_\sigma}\left((1-k)f - \frac{k}{2\pi}\frac{\partial \phi_1}{\partial \xi}(\xi,\eta), \frac{k}{2\pi}\frac{\partial \phi_1}{\partial \eta}(\xi,\eta)\right) + D \cdot M_\sigma(\phi_1)(\xi,\eta) \tag{21}$$

Theorem 2.1 suggests further simplification of $\Psi(\xi,\eta,0)$. We have indeed $\widehat{g_\sigma}(\xi,\eta) = e^{-2\pi^2\sigma^2(\xi^2+\eta^2)}$. Consequently, as soon as $\sigma f \geq 1$ and the partial derivatives of the phase maps satisfy $|\frac{\partial \phi_1}{\partial \xi}| << 2\pi f$ and $|\frac{\partial \phi_2}{\partial \eta}| << 2\pi f$, we have:

- $\widehat{g_\sigma}(f,0) = e^{-2\pi^2\sigma^2 f^2} < e^{-2\pi^2} \simeq 2.7\cdot 10^{-9}$
- $\sum_{k\in\mathbb{Z}^*} |d_k| \widehat{g_\sigma}(f - \frac{k}{2\pi}\frac{\partial \phi_2}{\partial \xi}, fk - \frac{k}{2\pi}\frac{\partial \phi_2}{\partial \eta}) \leq \left(\sum_{k\in\mathbb{Z}^*} |d_k|^2\right)^{1/2} \left(\sum_{k\in\mathbb{Z}^*} e^{-\sigma^2 k^2\left(2\pi f - \frac{\partial \phi_2}{\partial \eta}\right)^2}\right)^{1/2}$ with Cauchy-Schwartz inequality.

  Now, on the one hand,

  $$\begin{aligned}\sum_{k\in\mathbb{Z}^*} e^{-\sigma^2 k^2\left(2\pi f - \frac{\partial \phi_2}{\partial \eta}\right)^2} &\leq \sum_{k\in\mathbb{Z}^*} e^{-\sigma^2 |k|\left(2\pi f - \frac{\partial \phi_2}{\partial \eta}\right)^2} = 2\left(\sum_{k\geq 0} e^{-\sigma^2 k\left(2\pi f - \frac{\partial \phi_2}{\partial \eta}\right)^2} - 1\right)\\ &= \frac{2e^{-\sigma^2\left(2\pi f - \frac{\partial \phi_2}{\partial \eta}\right)^2)}}{1 - e^{-\sigma^2\left(2\pi f - \frac{\partial \phi_2}{\partial \eta}\right)^2}} \simeq 2e^{-4\pi^2\sigma^2 f^2} \simeq 5.4\cdot 10^{-9}\end{aligned}$$

  On the other hand, Parseval's theorem yields $\left(\sum_{k\in\mathbb{Z}^*} |d_k|^2\right)^{1/2} = ||\mathsf{frng}||_2$.

- In a similar way, $\sum_{k\neq 0,1} |d_k| \widehat{g_\sigma}((1-k)f - \frac{k}{2\pi}\frac{\partial \phi_1}{\partial \xi}, \frac{k}{2\pi}\frac{\partial \phi_1}{\partial \eta}) \leq \sum_{k\in\mathbb{Z}^*} e^{-\sigma^2 k^2\left(2\pi f + \frac{\partial \phi_1}{\partial \xi}\right)^2} \simeq 5.4\cdot 10^{-9}$.

Note that these numerical bounds are rather coarse. Assuming $\sigma f \geq 1$ basically means that the analysis window g_σ contains several line patterns of the grid.

Under these assumptions, we consider that:

$$\left\{\begin{array}{l} I_1(\xi,\eta) \simeq 0 \\ I_2'(\xi,\eta) \simeq D\cdot M_\sigma(\phi_1) \\ I_3(\xi,\eta) \simeq D\cdot M_\sigma(\phi_2)\end{array}\right. \tag{22}$$

Now, since $\iint x^2 g_\sigma(x,y)\ \mathrm{d}x\ \mathrm{d}y = \sigma^2$, $M_\sigma(\phi) \leq \sigma^2 M$, where M is an upper bound for the second order partial derivatives of ϕ "inside" the window g_σ. We also assume that these second order derivatives are negligible when compared to $g_\sigma * e^{i\phi_1}$. Note that even relatively large yet well-localized second order derivatives are smoothed out when computing M_σ from eq. (15).

We can remark that these simplifications benefit from well localized g_σ (in order to neglect $M_\sigma(\phi)$) and $\widehat{g_\sigma}$ (so that the terms with $\widehat{g_\sigma}(\cdot,\cdot)$ vanish.) This motivates us to use Gaussian windows, since it is well known [8, 15] that these windows realize the best compromise in the uncertainty principle.

We eventually get the following simplification, which is valid as soon as $\sigma f \geq 1$, $M_\sigma(\phi_1)$ and $M_\sigma(\phi_1)$ are negligible, and $|\partial\phi_1/\partial\xi|$ and $|\partial\phi_2/\partial\eta|$ are small with respect to $2\pi f$.

Approximation 1.

$$\Psi(x,y,0) \simeq \frac{\gamma A}{2} d_1 \iint g_\sigma(x-\xi, y-\eta) e^{i\phi_1(x,y)} \, \mathrm{d}x \, \mathrm{d}y \tag{23}$$

From approximation 1, we derive the following relation between the phases, denoting angle(z) the phase of the complex number $z \neq 0$. Since $\gamma A/2$ is a real number, we indeed have:

Approximation 1b.

$$\text{angle}\left(\Psi(x,y,0)\right) \simeq \text{angle}(d_1) + \text{angle}\left(\iint g_\sigma(x-\xi, y-\eta) e^{i\phi_1(x,y)} \, \mathrm{d}x \, \mathrm{d}y\right) \mod(2\pi) \tag{24}$$

Similarly to the $\Psi(\xi,\eta,0)$ case, under the same assumptions:

$$\text{angle}\left(\Psi(x,y,\pi/2)\right) \simeq \text{angle}(d_1) + \text{angle}\left(\iint g_\sigma(x-\xi, y-\eta) e^{i\phi_2(x,y)} \, \mathrm{d}x \, \mathrm{d}y\right) \mod(2\pi) \tag{25}$$

2.2.2 Phase of the Fourier transform

As a consequence of the following theorem, it turns out that the phase of the Fourier transform of the grid image can be approximately considered as the convolution product between the phase modulation ϕ and the window function g_σ.

Theorem 2.2 *If $\alpha_\sigma(\xi,\eta)$ is defined as:*

$$\alpha_\sigma(\xi,\eta) = \mathit{angle}\left(\iint g_\sigma(x-\xi, y-\eta) e^{i\phi_1(x,y)} \, dx \, dy\right) \tag{26}$$

Then:

$$|g_\sigma * \phi_1(\xi,\eta) - \alpha_\sigma(\xi,\eta)| \leq \frac{1}{6} \iint |\phi_1(x,y) - \alpha_\sigma(\xi,\eta)|^3 g_\sigma(x-\xi, y-\eta) \, dx \, dy. \tag{27}$$

Let us justify that this upper bound is practically very small and permits to approximate α_σ with $g_\sigma * \phi_1$. With Taylor's theorem:

$$\phi_1(x+\xi, y+\eta) = \phi_1(\xi,\eta) + <(x,y), \nabla\phi_1(\xi,\eta)> + \frac{1}{2}(x,y) \cdot H(\xi + h_1 x, \eta + h_2 y) \cdot (x,y)^T \tag{28}$$

as in eq. (16).

Plugging into eq. (26):

$$\begin{aligned} \alpha_\sigma(\xi,\eta) &= \text{angle}\left(e^{i\phi_1(\xi,\eta)} \iint g_\sigma(x,y) e^{i<(x,y),\nabla\phi_1(\xi,\eta)>} e^{\frac{i}{2}(x,y)H(x,y)^T} \, \mathrm{d}x \, \mathrm{d}y\right) & (29) \\ &= \phi_1(\xi,\eta) + \text{angle}\left(\iint g_\sigma(x,y) e^{i<(x,y),\nabla\phi_1(\xi,\eta)> + \frac{i}{2}(x,y)H(x,y)^T} \, \mathrm{d}x \, \mathrm{d}y\right) \mod(2\pi) & (30) \end{aligned}$$

Since for any complex z, a Taylor series expansion yields $e^{iz} = 1 + z \cdot \gamma(z)$ with $|\gamma| \leq 1$:

$$\begin{aligned}\iint g_\sigma(x,y) e^{i<(x,y),\nabla\phi_1(\xi,\eta)> + \frac{i}{2}(x,y)H(x,y)^T} \, \mathrm{d}x \, \mathrm{d}y = 1 + \\ \iint g_\sigma(x,y) \left(< (x,y), \nabla\phi_1(\xi,\eta) > + \frac{1}{2}(x,y)H(x,y)^T \right) \gamma(x,y,\xi,\eta) \, \mathrm{d}x \, \mathrm{d}y\end{aligned} \tag{31}$$

because g_σ integrates to 1. Now,

$$\begin{aligned}\left| \iint g_\sigma(x,y) \left(< (x,y), \nabla\phi_1(\xi,\eta) > + \frac{1}{2}(x,y)H(x,y)^T \right) \gamma(x,y,\xi,\eta) \, \mathrm{d}x \, \mathrm{d}y \right| \leq \\ \iint |x| g_\sigma(x,y) \, \mathrm{d}x \, \mathrm{d}y \cdot \left(|\frac{\partial\phi_1}{\partial\xi}(\xi,\eta)| + |\frac{\partial\phi_1}{\partial\eta}(\xi,\eta)| \right) + \frac{1}{2} M_\sigma(\phi_1)\end{aligned} \tag{32}$$

Note that $\iint |x| g_\sigma(x,y) \, \mathrm{d}x \, \mathrm{d}y = \frac{\sigma}{2\pi}$.

Assuming that $z \in \mathbb{C}$ is such that $|z|$ is much smaller than 1, then $\arctan(1+z) \simeq |z|$. Hence

$$|\alpha_\sigma(\xi,\eta) - \phi_1(\xi,\eta)| \simeq \frac{\sigma}{2\pi} \left(|\frac{\partial\phi_1}{\partial\xi}(\xi,\eta)| + |\frac{\partial\phi_1}{\partial\eta}(\xi,\eta)| \right) + \frac{1}{2} M_\sigma(\phi_1) \tag{33}$$

Let us note $\mathcal{I} = \iint |\phi_1(x+\xi, y+\eta) - \alpha_\sigma(\xi,\eta)|^3 g_\sigma(x,y) \, \mathrm{d}x \, \mathrm{d}y$. With Minkowski's inequality:

$$\begin{aligned}\mathcal{I}^{1/3} \leq \left(\iint |\phi_1(x+\xi, y+\eta) - \phi_1(\xi,\eta)|^3 g_\sigma(x,y) \, \mathrm{d}x \, \mathrm{d}y \right)^{1/3} \\ + \left(\iint |\phi_1(\xi,\eta) - \alpha_\sigma(\xi,\eta)|^3 g_\sigma(x,y) \, \mathrm{d}x \, \mathrm{d}y \right)^{1/3}\end{aligned} \tag{34}$$

With eq. (33), since g_σ integrates to 1:

$$\mathcal{I}^{1/3} \leq \frac{\sigma}{2\pi} \left(|\frac{\partial\phi_1}{\partial\xi}(\xi,\eta)| + |\frac{\partial\phi_1}{\partial\eta}(\xi,\eta)| \right) + \frac{1}{2} M_\sigma(\phi_1) \tag{35}$$

With eq. (28) and noting that, with the same z and assumption as above, $|z|^3 < |z|$:

$$\mathcal{I}^{1/3} \leq \left(\iint |\phi_1(x+\xi, y+\eta) - \phi_1(\xi,\eta)| g_\sigma(x,y) \, \mathrm{d}x \, \mathrm{d}y \right)^{1/3} \tag{36}$$

$$\leq \left(\frac{\sigma}{2\pi} \left(\left|\frac{\partial\phi_1}{\partial\xi}(\xi,\eta)\right| + \left|\frac{\partial\phi_1}{\partial\eta}(\xi,\eta)\right| \right) + \frac{1}{2} M_\sigma(\phi_1) \right)^{1/3} \tag{37}$$

Consequently:

$$|g_\sigma * \phi_1(\xi,\eta) - \alpha_\sigma(\xi,\eta)| \leq \frac{\sigma}{6\pi} \left(\left|\frac{\partial\phi_1}{\partial\xi}(\xi,\eta)\right| + \left|\frac{\partial\phi_1}{\partial\eta}(\xi,\eta)\right| \right) + \frac{1}{6} M_\sigma(\phi_1) \tag{38}$$

In addition to the hypothesis of Approximation 1, we also assume $\sigma||\nabla\phi||$ small enough. A trade-off appears: while we need σ large enough so that Approximation 1 holds, if $||\nabla\phi||$ becomes locally quite large, then the range of σ should be limited. Approximating $\alpha_\sigma(\xi,\eta)$ with $g_\sigma * \phi_1(\xi,\eta)$ allows us to further simplify Approximation 1b into:

Approximation 2.

$$\text{angle}\left(\Psi(\xi,\eta,0)\right) \simeq \text{angle}(d_1) + \iint g_\sigma * \phi_1(\xi,\eta) \mod(2\pi) \tag{39}$$

and similarly:

$$\text{angle}\left(\Psi(\xi,\eta,\pi/2)\right) \simeq \text{angle}(d_1) + \iint g_\sigma * \phi_2(\xi,\eta) \mod(2\pi) \tag{40}$$

The validity of this informal discussion and of these approximations has yet to be numerically assessed.

2.2.3 Derivatives of the phase

The physical quantity of interest is actually the strain components, that is, from eq. (3), the derivatives of the phase. We prove a theorem similar to theorem 2.2 dedicated to the phase derivatives. Since we compute the phase derivative of a complex function $z(t) = x(t) + iy(t)$ by $\mathrm{d}/\,\mathrm{d}t\big(\arctan(y/x)\big) = (y'x - yx')/|z|^2 = \mathrm{Im}(z'\overline{z})/|z|^2$, it is not sensitive to phase wrapping.

Theorem 2.3 *With the same notations as in theorem 2.2, we have:*

$$\begin{gathered}\left| g_\sigma * \frac{\partial \phi_1}{\partial \xi}(\xi,\eta) - \frac{\partial \alpha_\sigma}{\partial \xi}(\xi,\eta)\right| \leq \\ \frac{1}{2}\iint |\phi_1(x,y) - \alpha_\sigma(\xi,\eta)|^2 \left|\frac{\partial \phi_1}{\partial \xi}(x,y) - \frac{\partial \alpha_\sigma}{\partial \xi}(\xi,\eta)\right| g_\sigma(x-\xi, y-\eta)\; dx\; dy\end{gathered} \tag{41}$$

We do not derive further an approximation of $\left|\frac{\partial \phi_1}{\partial \xi}(x,y) - \frac{\partial \alpha_\sigma}{\partial \xi}(\xi,\eta)\right|$, but as in section 2.2.2, the point is that the variations of $\frac{\partial \phi_1}{\partial \xi}(x,y)$ are limited inside the window g_σ, which holds because $M_\sigma(\phi_1)$ is negligible. Based on this assumption, it is possible to approximate the phase derivatives.

Approximation 3.

$$\frac{\partial}{\partial \xi}\text{angle}\left(\Psi(\xi,\eta,0)\right) \simeq g_\sigma * \frac{\partial \phi_1}{\partial \xi}(\xi,\eta) \mod(2\pi) \tag{42}$$

and:

$$\frac{\partial}{\partial \eta}\text{angle}\left(\Psi(\xi,\eta,0)\right) \simeq g_\sigma * \frac{\partial \phi_1}{\partial \eta}(\xi,\eta) \mod(2\pi) \tag{43}$$

and the same holds for the derivatives of $\text{angle}\left(\Psi(x,y,\pi/2)\right)$ and of ϕ_2:

$$\frac{\partial}{\partial \xi}\text{angle}\left(\Psi(\xi,\eta,\pi/2)\right) \simeq g_\sigma * \frac{\partial \phi_2}{\partial \xi}(\xi,\eta) \mod(2\pi) \tag{44}$$

and:

$$\frac{\partial}{\partial \eta}\text{angle}\left(\Psi(\xi,\eta,\pi/2)\right) \simeq g_\sigma * \frac{\partial \phi_2}{\partial \eta}(\xi,\eta) \mod(2\pi) \tag{45}$$

2.2.4 Summary

Assuming that σf is larger than 1, that the derivatives of the phase maps ϕ_1 and ϕ_2 are small with respect to $2\pi f$, and that the second order derivatives are locally limited inside the analysis windows g_σ, then Approximation 1b holds (eq. (24) and (25)). Further assuming that $\sigma||\nabla\phi_1||$ and $\sigma||\nabla\phi_2||$ are small, then Approximation 2 (eq. (39) and (40)) and Approximation 3 (eq. (42) to (45)) hold.

This discussion will be illustrated in section 4 on typical values from practical cases. As we will see, $M_\sigma(\phi_1)$ and $M_\sigma(\phi_2)$ yield very limited artifacts.

As an example, $1/f$ is typically equal to some tens of mm. A typical value is 0.2 mm. Since 5 pixels/mm are classically employed to encode one grid pitch, it means that $1/f$=5 pixels in this case, each pixel of the CCD chip corresponding to $40 \cdot 10^{-3}$ mm on the specimen. In the case of small deformations, strain components may reach up to some percents and thus phase derivatives some tenths of m^{-1} since strains are merely equal to phase derivatives times $-1/(2\pi f)$. With σ around 0.2 mm, $\sigma|\nabla\phi_i|$ is hence below $10^{-2} - 10^{-3}$.

2.3 Proofs of the theorems

To the very best of our knowledge, theorems 2.1, 2.2 and 2.3 are not special cases of standard results connecting the windowed Fourier transform and the phase of an analytic signal $A(x)e^{i\phi(x)}$ (either in the signal processing literature [8, 9, 15] or in the fringe pattern analysis literature [14, 17].) We therefore propose a dedicated self-contained proof in this section. Our study is specific in that the frequency f of the carrier is known from the experimental setting.

2.3.1 Proof of theorem 2.1

For this demonstration, we take our inspiration from the demonstration of theorem 4.4.1 in [15, pp.94-95] which holds in the 1D case.

With the notations of section 2.1 and from eq. (1) and (4):

$$\begin{aligned}
\Psi(\xi,\eta,0) &= \iint s(x,y) g_\sigma(x-\xi,y-\eta) e^{-i2\pi f x}\,\mathrm{d}x\,\mathrm{d}y &(46)\\
&= A I_1(\xi,\eta) + \frac{\gamma A}{2} I_2(\xi,\eta) + \frac{\gamma A}{2} I_3(\xi,\eta). &(47)
\end{aligned}$$

Let us begin with I_1. With proposition A.1 in appendix:

$$\begin{aligned}
|I_1(\xi,\eta)| &= \left| \iint g_\sigma(x-\xi,y-\eta) e^{-2i\pi f x}\,\mathrm{d}x\,\mathrm{d}y \right| &(48)\\
&= |\widehat{g_\sigma}(f,0)| &(49)
\end{aligned}$$

This proves eq. (18).

Let us now bound I_3. From the Fourier decomposition of the frng function (eq. (14)):

$$\mathsf{frng}(2\pi f y + \phi_2(x,y)) = \sum_{k\in\mathbb{Z}^*} d_k e^{2i\pi f k y + ik\phi_2(x,y)} \tag{50}$$

Plugging eq. (50) in eq. (12) and reorganizing yields:

$$I_3(\xi,\eta) = \sum_{k\in\mathbb{Z}^*} d_k \iint g_\sigma(x-\xi,y-\eta) e^{-2i\pi(fx - fky)} e^{ik\phi_2(x,y)}\,\mathrm{d}x\,\mathrm{d}y \tag{51}$$

Now, from Taylor's theorem (see proposition A.3):

$$\phi_2(x,y) = \phi_2(\xi,\eta) + < (x-\xi,y-\eta), \nabla\phi_2(\xi,\eta) > + \frac{1}{2}(x-\xi,y-\eta) H(\delta) (x-\xi,y-\eta)^T \tag{52}$$

where $H(x,y)$ is the Hessian matrix of ϕ_2 at (x,y) and δ belongs to the line segment connecting $[\xi,\eta]$ and $[x,y]$ (we assume that ϕ_2 is C^2 around (ξ,η).)

By substituting the expression of $\phi_2(x,y)$ from this latest equation into eq. (51), and with the changes of variables $x \leftarrow x-\xi$ and $y \leftarrow y-\eta$:

$$\begin{aligned} I_3(\xi,\eta) = &\sum_{k\in\mathbb{Z}^*} d_k e^{ik\phi_2(\xi,\eta)-2i\pi f(\xi-k\eta)} \\ &\cdot \iint g_\sigma(x,y) e^{-2i\pi(fx-fky)+ik<(x,y),\nabla\phi_2>} e^{ik(x,y)H(\delta)(x,y)(x,y)^T/2}\,\mathrm{d}x\,\mathrm{d}y \end{aligned} \tag{53}$$

A Taylor series expansion of e^{it} yields $e^{it}=1+t\gamma(t)$ with $|\gamma|\leq 1$. Thus:

$$e^{ik(x,y)H(\delta)(x,y)^T/2} = 1+\frac{1}{2}k(x,y)H(\delta)(x,y)^T\gamma \tag{54}$$

With triangle inequality:

$$\begin{aligned} |I_3(\xi,\eta)| \leq &\sum_{k\in\mathbb{Z}^*} |d_k| \widehat{g_\sigma}\left(f-\frac{k}{2\pi}\frac{\partial\phi_2}{\partial\xi}, fk-\frac{k}{2\pi}k\frac{\partial\phi_2}{\partial\eta}\right) \\ &+\frac{1}{2}\sum_{k\in\mathbb{Z}^*}|kd_k| \iint \left|(x,y)\mathcal{H}^{(\xi,\eta)}_{(x,y)}\right| g_\sigma(x,y)\,\mathrm{d}x\,\mathrm{d}y \end{aligned} \tag{55}$$

with $\mathcal{H}^{(\xi,\eta)}_{(x,y)}$ as in eq. (17).

This proves eq. (19).

Now we deal with the bound on I_2. From the definition of I_2 and the Fourier series expansion of frng:

$$I_2(\xi,\eta) = \iint \sum_{k\in\mathbb{Z}^*} d_k e^{2i\pi fkx+ik\phi_1(x,y)} g_\sigma(x-\xi,y-\eta)e^{-2i\pi fx}\,\mathrm{d}x\,\mathrm{d}y \tag{56}$$

$$= \sum_{k\in\mathbb{Z}^*} d_k \iint g_\sigma(x-\xi,y-\eta)e^{-2i\pi(1-k)fx}e^{ik\phi_1(x,y)}\,\mathrm{d}x\,\mathrm{d}y \tag{57}$$

Hence:

$$\begin{aligned} I_2(\xi,\eta) = &\sum_{k\neq 0,1} d_k \iint g_\sigma(x-\xi,y-\eta)e^{-2i\pi(1-k)fx}e^{ik\phi_1(x,y)}\,\mathrm{d}x\,\mathrm{d}y \\ &+ d_1 \iint g_\sigma(x-\xi,y-\eta)e^{i\phi_1(x,y)}\,\mathrm{d}x\,\mathrm{d}y \end{aligned} \tag{58}$$

Let us note:

$$I_2'(\xi,\eta) = \sum_{k\neq 0,1} d_k \iint g_\sigma(x-\xi,y-\eta)e^{-2i\pi(1-k)fx}e^{ik\phi_1(x,y)}\,\mathrm{d}x\,\mathrm{d}y \tag{59}$$

With a Taylor series expansion of $\phi_1(x,y)$ and the same arguments as in eq. (55), we derive the following upper bound on I_2':

$$\begin{aligned} |I_2'(\xi,\eta)| \leq &\sum_{k\neq 0,1} |d_k| |\widehat{g_\sigma}\left((1-k)f-\frac{k}{2\pi}\frac{\partial|\phi_1}{\partial\xi}, \frac{k}{2\pi}\frac{\partial\phi_1}{\partial\eta}\right) \\ &+\frac{1}{2}\sum_{k\neq 0,1}|kd_k| \iint \left|(x,y)\mathcal{H}^{\xi,\eta}_{(x,y)}(x,y)\right| g_\sigma(x,y)\,\mathrm{d}x\,\mathrm{d}y \end{aligned} \tag{60}$$

where $\mathcal{H}^{\xi,\eta}_{(x,y)}$ is an upper bound of the Hessian matrix of ϕ_1 on the segment line between $[\xi,\eta]$ and $[x,y]$.

This proves eq. (21), and completes the proof of theorem 2.1.

2.3.2 Proof of theorem 2.2

Let us note $N_\sigma(\xi,\eta)$ the modulus and $\alpha_\sigma(\xi,\eta)$ the phase of $\iint g_\sigma(x-\xi,y-\eta)e^{i\phi_1(x,y)}\,\mathrm{d}x\,\mathrm{d}y$.
In this section we use the following lemma:

Lemma 2.4 *The following equalities hold:*

$$\iint g_\sigma(x-\xi,y-\eta)\cos(\phi_1(x,y)-\alpha_\sigma(\xi,\eta))\;dx\;dy = N_\sigma(\xi,\eta) \tag{61}$$

$$\iint g_\sigma(x-\xi,y-\eta)\sin(\phi_1(x,y)-\alpha_\sigma(\xi,\eta))\;dx\;dy = 0 \tag{62}$$

Proof. By definition:

$$\iint g_\sigma(x-\xi,y-\eta)e^{i\phi_1(x,y)}\,\mathrm{d}x\,\mathrm{d}y = N_\sigma(\xi,\eta)e^{i\alpha_\sigma(\xi,\eta)} \tag{63}$$

Hence,

$$N_\sigma(\xi,\eta) = \iint g_\sigma(x-\xi,y-\eta)e^{i(\phi_1(x,y)-\alpha_\sigma(\xi,\eta))}\,\mathrm{d}x\,\mathrm{d}y \tag{64}$$

The result is obtained by taking real and imaginary parts. □

Now, a Taylor series expansion gives:

$$\sin(\phi_1(x,y)-\alpha_\sigma(\xi,\eta)) = \phi_1(x,y)-\alpha_\sigma(\xi,\eta) - \frac{1}{6}(\phi_1(x,y)-\alpha_\sigma(\xi,\eta))^3\gamma(x,y,\xi,\eta) \tag{65}$$

where $|\gamma| \leq 1$.

By multiplying eq. (65) by $g_\sigma(x-\xi,y-\eta)$ and integrating with respect to x and y, we obtain with lemma 2.4 (eq. (62)):

$$\begin{aligned} 0 = \iint g_\sigma(x-\xi,y-\eta)\phi_1(x,y)\,\mathrm{d}x\,\mathrm{d}y - \alpha_\sigma(\xi,\eta) \\ -\frac{1}{6}\iint g_\sigma(x-\xi,y-\eta)|\phi_1(x,y)-\alpha_\sigma(\xi,\eta))^3\gamma(x,y,\xi,\eta)\,\mathrm{d}x\,\mathrm{d}y \end{aligned} \tag{66}$$

With triangle inequality:

$$\left|\iint g_\sigma(x-\xi,y-\eta)\phi_1(x,y)\,\mathrm{d}x\,\mathrm{d}y - \alpha_\sigma(\xi,\eta)\right| \leq \frac{1}{6}\iint |\phi_1(x,y)-\alpha_\sigma(\xi,\eta)|^3 g_\sigma(x-\xi,y-\eta)\,\mathrm{d}x\,\mathrm{d}y \tag{67}$$

2.3.3 Proof of theorem 2.3

By definition:

$$N_\sigma(\xi,\eta)e^{i\alpha_\sigma(\xi,\eta)} = \iint g_\sigma(x-\xi,y-\eta)e^{i\phi_1(x,y)}\,\mathrm{d}x\,\mathrm{d}y = \iint g_\sigma(x,y)e^{i\phi_1(x+\xi,y+\eta)}\,\mathrm{d}x\,\mathrm{d}y \tag{68}$$

A derivation yields:

$$\frac{\partial N_\sigma}{\partial \xi}(\xi,\eta)e^{i\alpha_\sigma(\xi,\eta)} + iN_\sigma(\xi,\eta)\frac{\partial \alpha_\sigma(\xi,\eta)}{\partial \xi}e^{i\alpha_\sigma(\xi,\eta)} = i\iint g_\sigma(x-\xi,y-\eta)\frac{\partial \phi_1}{\partial \xi}(x,y)e^{i\phi_1(x,y)}\,\mathrm{d}x\,\mathrm{d}y \tag{69}$$

Hence, multiplying by $e^{-i\alpha_\sigma(\xi,\eta)}$ and taking the imaginary part:

$$N_\sigma(\xi,\eta)\frac{\partial \alpha_\sigma}{\partial \xi}(\xi,\eta) = \iint g_\sigma(x-\xi,y-\eta)\frac{\partial \phi_1}{\partial \xi}(x,y)\cos(\phi_1(x,y)-\alpha_\sigma(\xi,\eta))\,\mathrm{d}x\,\mathrm{d}y \tag{70}$$

Plugging the expression of $N_\sigma(\xi,\eta)$ from lemma 2.4 (eq. (61)) in the left-hand term of eq. (70):

$$\iint g_\sigma(x-\xi,y-\eta)\left(\frac{\partial \phi_1}{\partial \xi}(x,y) - \frac{\partial \alpha_\sigma}{\partial \xi}(\xi,\eta)\right)\cos(\phi_1(x,y)-\alpha_\sigma(\xi,\eta))\,\mathrm{d}x\,\mathrm{d}y = 0 \tag{71}$$

Now, a Taylor expansion yields:

$$\cos(\phi_1(x,y)-\alpha_\sigma(\xi,\eta)) = 1 - \frac{1}{2}(\phi_1(x,y)-\alpha_\sigma(\xi,\eta))^2\cos(h(\phi_1(x,y)-\alpha_\sigma(\xi,\eta)) \tag{72}$$

where $h \in [0,1]$.

Consequently, since g_σ integrates to 1, we get by plugging eq. (72) into (71):

$$\begin{gathered}\left|\iint g_\sigma(x-\xi,y-\eta)\frac{\partial \phi_1}{\partial x}(x,y)\,\mathrm{d}x\,\mathrm{d}y - \frac{\partial \alpha_\sigma}{\partial \xi}(\xi,\eta)\right| \leq \\ \frac{1}{2}\iint |\phi_1(x,y)-\alpha_\sigma(\xi,\eta)|^2\left|\frac{\partial \phi_1}{\partial x}(x,y) - \frac{\partial \alpha_\sigma}{\partial \xi}(\xi,\eta)\right| g_\sigma(x-\xi,y-\eta)\,\mathrm{d}x\,\mathrm{d}y\end{gathered} \tag{73}$$

which proves theorem 2.3.

3 The realistic, sampled/quantized and noisy model

Section 2 suggests that in the grid method, the phase (resp. the phase derivatives) measured from the windowed Fourier transform is approximately the convolution of the actual phase (resp. the actual phase derivatives) with the window function g_σ under mild assumptions. An appealing idea is to use deconvolution to recover the actual phase (resp. the actual phase derivatives) from eq. (39) and (40) (approximation 2), resp. eq. (42) and (43) (approximation 3). However, the noise in the grid image cannot totally be ignored, although the output of the CCD which is used has a high signal / noise ratio. Here, deconvolution will have to take noise into account, as demonstrated in [11]. In this section we study how a Gaussian white noise transfers from the grid image to the phase or phase derivative maps.

We assume that the grid image is given with an additive pixel-wise noise:

$$\widetilde{s}(x,y) = s(x,y) + n(x,y) \tag{74}$$

where $\widetilde{s}(x,y)$ is the observed image, s is the ideal, noise-free image, and $n(x,y)$ is a random noise.

The observed image s is actually sampled (along the x- and y- axis) and quantized (the gray-scale range is finite). For example, the camera employed to obtain the strain maps shown in figure 1 is a Sensicam-QE one which exhibits a 12-bit/1040×1376-pixel sensor.

We will assume sampling to be fine enough so that Shannon-Nyquist conditions [15] are practically satisfied and aliasing effects are not perceived on the frequency band of interest.

Note that the signal of interest is most likely not band-limited, so rigorously aliasing cannot be avoided. Quantization also makes it impossible, even with a noise-free image, to perfectly recover the actual phase from the grid image within the framework of section 2. We will not discuss further the effects of sampling and quantization in this report.

Section 3.1 investigates how the windowed Fourier transform acts on noise. Section 3.2 then gives an approximation of the noise on the phase and phase derivative maps.

In this section, we note $\mathrm{Re}(z)$ and $\mathrm{Im}(z)$ the real and imaginary parts of a complex number z, respectively.

3.1 Windowed Fourier transform of a Gaussian white noise

In the presence of noise, $\Psi(\xi,\eta,\theta)$ transforms into $\widetilde{\Psi}(\xi,\eta,\theta)$ which is defined as follows:

$$\widetilde{\Psi}(\xi,\eta,\theta) = \Psi(\xi,\eta,\theta) + \sum_{i,j} n(x_i,y_j) g_\sigma(x_i-\xi, y_j-\eta) e^{-2i\pi f(x_i\cos(\theta)+y_j\sin(\theta))}\Delta_x\Delta_y \tag{75}$$

where Ψ is the ideal, noise-free Fourier transform, and $(x_i,y_j) = (x'_i\Delta_x, y'_i\Delta_y)$ where (Δ_x,Δ_y) is the grid pitch in the image s (here $\Delta_x = \Delta_y = 1$ pixel, thus typically $40\cdot 10^{-3}$ mm on the specimen surface if 5 pixels per grid period are used to encode a grid featuring 5 lines per mm.)

We assume that n is a Gaussian white noise with mean 0 and variance v.

Let us focus on $\widetilde{\Psi}(\xi,\eta,0)$ and note:

$$\widehat{n}(\xi,\eta) = \sum_{i,j} n(x_i,y_j) g_\sigma(x_i-\xi, y_j-\eta) e^{-2i\pi f x_i}\Delta_x\Delta_y \tag{76}$$

Since n is a Gaussian white noise, then $\widehat{n}(\xi,\eta)$ is a (complex) Gaussian random variable for every (ξ,η). Let us characterize it more precisely.

Proposition 3.1 *The covariance and autocovariance of the real and imaginary parts of $\widehat{n}$ (defined as in eq. 76) are:*

$$Covar(Re(\widehat{n}(\xi,\eta)), Re(\widehat{n}(\xi',\eta'))) \simeq \frac{v\Delta_x\Delta_y}{8\pi\sigma^2} e^{-(\xi-\xi')^2/(4\sigma^2)-(\eta-\eta')^2/(4\sigma^2)}\left(1+e^{-4\pi^2\sigma^2f^2}\cos(2\pi f(\xi+\xi')\right) \tag{77}$$

$$Covar(Im(\widehat{n}(\xi,\eta)), Im(\widehat{n}(\xi',\eta'))) \simeq \frac{v\Delta_x\Delta_y}{8\pi\sigma^2} e^{-(\xi-\xi')^2/(4\sigma^2)-(\eta-\eta')^2/(4\sigma^2)}\left(1-e^{-4\pi^2\sigma^2f^2}\cos(2\pi f(\xi+\xi')\right) \tag{78}$$

$$Covar(Re(\widehat{n}(\xi,\eta)), Im(\widehat{n}(\xi',\eta'))) \simeq \frac{v\Delta_x\Delta_y}{8\pi\sigma^2} e^{-(\xi-\xi')^2/(4\sigma^2)-(\eta-\eta')^2/(4\sigma^2)}\sin(2\pi f(\xi+\xi'))e^{-4\pi^2\sigma^2f^2} \tag{79}$$

The approximations come from replacing discrete Riemann sums with the corresponding integrals. We assess in section 4 that they are tight enough for the typical values of σ.

Proof. Let us note E the expectation of any random variable. Since n is a white noise of variance v, $E(n(x_i,y_j)n(x_k,y_l)) = 0$ if $x_i \neq x_k$ or $y_j \neq y_l$, and $= v$ otherwise.

Then, by expanding the real and imaginary parts of $\widehat{n}$ and replacing the discrete Riemann sums by integrals:

$$\begin{aligned}\mathrm{Covar}(\mathrm{Re}(\widehat{n}(\xi,\eta)),\mathrm{Re}(\widehat{n}(\xi',\eta'))) = & \quad v\sum_{i,j} g_\sigma(x_i-\xi,y_j-\eta)g_\sigma(x_i-\xi',y_j-\eta') \\ & \cdot\cos^2(2\pi f x_i)(\Delta_x\Delta_y)^2 \qquad (80)\\ \simeq & \quad v\Delta_x\Delta_y \iint g_\sigma(x-\xi,y-\eta)g_\sigma(x-\xi',y-\eta') \\ & \cdot\cos^2(2\pi f x)\,\mathrm{d}x\,\mathrm{d}y \qquad (81)\end{aligned}$$

and eq. (77) yields from proposition B.2, eq. (128) in appendix.

$$\begin{aligned}\mathrm{Covar}(\mathrm{Im}(\widehat{n}(\xi,\eta)),\mathrm{Im}(\widehat{n}(\xi',\eta'))) = & \quad v\sum_{i,j} g_\sigma(x_i-\xi,y_j-\eta)g_\sigma(x_i-\xi',y_j-\eta') \\ & \cdot\sin^2(2\pi f x_i)(\Delta_x\Delta_y)^2 \qquad (82)\\ \simeq & \quad v\Delta_x\Delta_y \iint g_\sigma(x-\xi,y-\eta)g_\sigma(x-\xi',y-\eta') \\ & \cdot\sin^2(2\pi f x)\,\mathrm{d}x\,\mathrm{d}y \qquad (83)\end{aligned}$$

and eq. (78) yields from proposition B.2, eq. (129) in appendix.

$$\begin{aligned}\mathrm{Covar}(\mathrm{Re}(\widehat{n}(\xi,\eta)),\mathrm{Im}(\widehat{n}(\xi',\eta'))) = & \quad v\sum_{i,j} g_\sigma(x_i-\xi,y_j-\eta)g_\sigma(x_i-\xi',y_j-\eta') \\ & \cdot\cos(2\pi f x_i)\sin(2\pi f x_i)(\Delta_x\Delta_y)^2 \qquad (84)\\ \simeq & \quad v\Delta_x\Delta_y \iint g_\sigma(x-\xi,y-\eta)g_\sigma(x-\xi',y-\eta') \\ & \cdot\cos(2\pi f x)\sin(2\pi f x)\,\mathrm{d}x\,\mathrm{d}y \qquad (85)\end{aligned}$$

and eq. (79) yields from proposition B.2, eq. (130) in appendix. □

As a corollary of proposition 3.1, setting $\xi = \xi'$ and $\eta = \eta'$ in eq. (77,78,79) yields:

Proposition 3.2 *The variance and covariances of real and imaginary parts of* $\widehat{n}$ *are:*

$$Var(Re(\widehat{n}(\xi,\eta))) \simeq \frac{v\Delta_x\Delta_y}{8\pi\sigma^2}\left(1+e^{-4\pi^2\sigma^2 f^2}\cos(4\pi f\xi)\right) \qquad (86)$$

$$Var(Im(\widehat{n}(\xi,\eta))) \simeq \frac{v\Delta_x\Delta_y}{8\pi\sigma^2}\left(1-e^{-4\pi^2\sigma^2 f^2}\cos(4\pi f\xi)\right) \qquad (87)$$

$$Covar(Re(\widehat{n}(\xi,\eta)),Im(\widehat{n}(\xi,\eta))) \simeq \frac{v\Delta_x\Delta_y}{8\pi\sigma^2}\sin(4\pi f\xi)e^{-4\pi^2\sigma^2 f^2} \qquad (88)$$

We can further simplify proposition 3.1 under the hypothesis of section 2. Assuming $\sigma f \geq 1$, we simplify the variances and covariances indeed into:

$$\mathrm{Var}(\mathrm{Re}(\widehat{n}(\xi,\eta))) = \mathrm{Var}(\mathrm{Im}(\widehat{n}(\xi,\eta))) = \frac{v\Delta_x\Delta_y}{8\pi\sigma^2} \qquad (89)$$

$$\mathrm{Covar}(\mathrm{Re}(\widehat{n}(\xi,\eta)),\mathrm{Im}(\widehat{n}(\xi',\eta'))) = 0 \tag{90}$$

$$\begin{aligned}\mathrm{Covar}(\mathrm{Re}(\widehat{n}(\xi,\eta)),\mathrm{Re}(\widehat{n}(\xi',\eta'))) &= \mathrm{Covar}(\mathrm{Im}(\widehat{n}(\xi,\eta)),\mathrm{Im}(\widehat{n}(\xi',\eta')))\\ &= \frac{v\Delta_x\Delta_y}{8\pi\sigma^2}e^{-(\xi-\xi')^2/(4\sigma^2)-(\eta-\eta')^2/(4\sigma^2)}\end{aligned} \tag{91}$$

This means that in practice, the real and imaginary parts of $\widehat{n}$ are uncorrelated Gaussian variables, and that they are both wide-sense stationary processes (indeed, in this case the auto-covariances only depend on $\xi-\xi'$ and $\eta-\eta'$.)

Qualitatively, the windowed Fourier transform diminishes the effect on $\widehat{\Psi}$ of the image grid noise, proportionally to the size of the window function on average (from eq. (86) and (87)). However, it also transforms the white noise in a correlated noise which creates "blob"-like shapes in $\Psi(\xi,\eta,0)$ with a size proportional to σ.

3.2 Effect of the image noise on the phase and its derivatives.

The noise n will affect the phase ϕ at every pixel (ξ,η). However, if the Signal-to-Noise Ratio (SNR) is large, then the modification is limited and the noise on the phase maps or on the phase derivatives can be accurately estimated.

3.2.1 Noise on the phase

The measured phase $\widetilde{\phi_1}(\xi,\eta)\in[0,2\pi]$ is from eq. (75-76):

$$\widetilde{\phi_1}(\xi,\eta) = \arctan\left(\frac{\mathrm{Im}(\Psi(\xi,\eta,0))+\mathrm{Im}(\widehat{n}(\xi,\eta))}{\mathrm{Re}(\Psi(\xi,\eta,0))+\mathrm{Re}(\widehat{n}(\xi,\eta))}\right) \tag{92}$$

If the noise variance is low with respect to $|\Psi(\xi,\eta,0)|$, then it is possible to neglect the effect of phase jumps due to noise, and to get an approximation of $\widetilde{\phi_1}$ via a Taylor expansion of arctan.

Indeed, since:

$$\arctan\left(\frac{y}{x}\right) = \arctan\left(\frac{y_0}{x_0}\right) - \frac{y_0}{x_0^2+y_0^2}(x-x_0) + \frac{x_0}{x_0^2+y_0^2}(y-y_0) + o\left(||(x-x_0,y-y_0)||_2\right) \tag{93}$$

we get (with $x_0=\mathrm{Re}(\Psi(\xi,\eta,0))$, $y_0=\mathrm{Im}(\Psi(\xi,\eta,0))$, $x=\mathrm{Re}(\widetilde{\Psi}(\xi,\eta,0))$, and $y=\mathrm{Im}(\widetilde{\Psi}(\xi,\eta,0))$):

$$\widetilde{\phi_1}(\xi,\eta) \simeq \mathrm{angle}(\Psi(\xi,\eta,0)) - \frac{\mathrm{Im}(\Psi(\xi,\eta,0))}{|\Psi(\xi,\eta,0)|^2}\mathrm{Re}(\widehat{n})(\xi,\eta) + \frac{\mathrm{Re}(\Psi(\xi,\eta,0))}{|\Psi(\xi,\eta,0)|^2}\mathrm{Im}(\widehat{n})(\xi,\eta) \tag{94}$$

Assuming $\sigma f\geq 1$, section 3.1 proves that real and imaginary parts of $\widehat{n}(\xi,\eta)$ can be considered as independent 0-mean Gaussian variables, with variance $v\Delta_x\Delta_y/(8\pi\sigma^2)$ (eq. (89) and (90)). However, these random variables are still spatially correlated (eq. 91). The phase becomes :

$$\widetilde{\phi_1}(\xi,\eta) \simeq \mathrm{angle}(\Psi(\xi,\eta,0)) + \widetilde{n}(\xi,\eta) \tag{95}$$

where $\widetilde{n}(\xi,\eta)$ is a Gaussian random variable with mean 0 and variance:

$$\mathrm{Var}(\widetilde{n}(\xi,\eta)) = \frac{\mathrm{Im}^2(\Psi(\xi,\eta,0))}{|\Psi(\xi,\eta,0)|^4}\mathrm{Var}(\mathrm{Re}(\widehat{n})) + \frac{\mathrm{Re}^2(\Psi(\xi,\eta,0))}{|\Psi(\xi,\eta,0)|^4}\mathrm{Var}(\mathrm{Im}(\widehat{n})) \tag{96}$$

$$= \frac{v\Delta_x\Delta_y}{8\pi\sigma^2|\Psi(\xi,\eta,0)|^2} \tag{97}$$

(see prop. A.2 in appendix.)

The autocovariance of $\widetilde{n}$ is:

$$\mathrm{Covar}(\widetilde{n}(\xi,\eta),\widetilde{n}(\xi',\eta')) = \left(\frac{\mathrm{Im}(\Psi(\xi,\eta,0))}{|\Psi(\xi,\eta,0)|^2}\frac{\mathrm{Im}(\Psi(\xi',\eta',0))}{|\Psi(\xi',\eta',0)|^2} + \frac{\mathrm{Re}(\Psi(\xi,\eta,0))}{|\Psi(\xi,\eta,0)|^2}\frac{\mathrm{Re}(\Psi(\xi',\eta',0))}{|\Psi(\xi',\eta',0)|^2}\right) \cdot \frac{v\Delta_x\Delta_y}{8\pi\sigma^2} e^{-(\xi-\xi')^2/(4\sigma^2)-(\eta-\eta')^2/(4\sigma^2)} \tag{98}$$

$$= \frac{\sin(\phi_1(\xi,\eta))\sin(\phi_1(\xi',\eta')) + \cos(\phi_1(\xi,\eta))\cos(\phi_1(\xi',\eta'))}{|\Psi(\xi,\eta,0)||\Psi(\xi',\eta',0)|} \cdot \frac{v\Delta_x\Delta_y}{8\pi\sigma^2} e^{-(\xi-\xi')^2/(4\sigma^2)-(\eta-\eta')^2/(4\sigma^2)} \tag{99}$$

$$= \frac{\cos(\phi_1(\xi,\eta)-\phi_1(\xi',\eta'))}{|\Psi(\xi,\eta,0)||\Psi(\xi',\eta',0)|}\frac{v\Delta_x\Delta_y}{8\pi\sigma^2} e^{-(\xi-\xi')^2/(4\sigma^2)-(\eta-\eta')^2/(4\sigma^2)} \tag{100}$$

Assuming that the phase variations are locally limited, the cosine is approximated by 1, and the covariance further simplifies into:

$$\mathrm{Covar}(\widetilde{n}(\xi,\eta),\widetilde{n}(\xi',\eta')) = \frac{v\Delta_x\Delta_y}{8\pi\sigma^2|\Psi(\xi,\eta,0)||\Psi(\xi',\eta',0)|} e^{-(\xi-\xi')^2/(4\sigma^2)-(\eta-\eta')^2/(4\sigma^2)} \tag{101}$$

Consequently, if Ψ can be considered as a constant (this will be discussed in section 3.2.3), then the noise $\widetilde{n}$ on the phase map can be practically considered as a wide-sense stationary process such that:

$$\mathrm{Covar}(\widetilde{n}(\xi,\eta),\widetilde{n}(\xi',\eta')) = \frac{v\Delta_x\Delta_y}{8\pi\sigma^2 P^2} e^{-(\xi-\xi')^2/(4\sigma^2)-(\eta-\eta')^2/(4\sigma^2)} \tag{102}$$

where $P = |\Psi(\cdot,\cdot,0)|$.

Note that the noise on the phase map ϕ_2 is the same as on ϕ_1, except for $P = |\Psi(\xi,\eta,\pi/2)|$.

Let us sum up. We have shown that, assuming $\sigma f \geq 1$, limited phase variations (so that the cosine in eq. (100) is $\simeq 1$) and Ψ constant, then the noise on the phase maps is a stationary 0-mean Gaussian process with variance given by eq. (97) and autocovariance by eq. (102).

3.2.2 Noise on the phase derivatives

Let us now discuss the influence of the image grid noise on the phase derivatives. We estimate the phase derivatives with the following equality, which holds based on the derivative of the arctan function:

$$\frac{\partial\phi_1}{\partial\cdot}(\xi,\eta) = \frac{\mathrm{Re}(\Psi(\xi,\eta,0))\frac{\partial \mathrm{Im}(\Psi)}{\partial\cdot}(\xi,\eta,0) - \mathrm{Im}(\Psi(\xi,\eta,0))\frac{\partial \mathrm{Re}(\Psi)}{\partial\cdot}(\xi,\eta,0)}{|\Psi(\xi,\eta,0)|^2} \tag{103}$$

where $\cdot$ denotes either ξ or η. Although a first order approximation as above would permit to estimate the noise on the phase derivatives, it yields painful equations. In our framework, it turns out that it is sufficient to consider from eq. (95) that the phase derivative is spoilt by the derivative of the random field $\widehat{n}'(\xi,\eta)$. For the sake of completeness, we compute the variance and autocovariance of the derived random field instead of making use of specific results of the literature (see e.g. [1].)

Let us remark that $\widetilde{n}(\xi+\delta,\eta)-\widetilde{n}(\xi,\eta)$ is a 0-mean random variable. It is not necessarily Gaussian because of the spatial correlations of $\widetilde{n}$. With eq. (89) to (91), we can develop its variance as:

$$\begin{aligned}\mathrm{Var}(\widetilde{n}(\xi+\delta,\eta)-\widetilde{n}(\xi,\eta)) = \frac{v\Delta_x\Delta_y}{8\pi\sigma^2}\Bigg(\frac{1}{|\Psi(\xi+\delta,\eta,0)|^2}+\frac{1}{|\Psi(\xi,\eta,0)|^2}\\ -2\frac{\mathrm{Re}(\Psi(\xi+\delta,\eta,0))\cdot\mathrm{Re}(\Psi(\xi,\eta,0))+\mathrm{Im}(\Psi(\xi+\delta,\eta,0))\cdot\mathrm{Im}(\Psi(\xi,\eta,0))}{|\Psi(\xi,\eta,0)|^2|\Psi(\xi+\delta,\eta,0)|^2}e^{-\delta^2/(4\sigma^2)}\Bigg)\end{aligned} \tag{104}$$

Hence:

$$\mathrm{Var}\left(\frac{\widetilde{n}(\xi+\delta,\eta)-\widetilde{n}(\xi,\eta)}{\delta}\right) \sim_{\delta\to 0} \frac{2v\Delta_x\Delta_y}{8\pi\sigma^2|\Psi(\xi,\eta,0)|^2}\frac{1-e^{-\delta^2/(4\sigma^2)}}{\delta^2} \tag{105}$$

$$\sim_{\delta\to 0} \frac{v\Delta_x\Delta_y}{16\pi\sigma^4|\Psi(\xi,\eta,0)|^2} \tag{106}$$

since $(1-e^{-\alpha x})/x\to\alpha$ when $x\to 0$.

Consequently, $\frac{\partial\widetilde{n}}{\partial\xi}(\xi,\eta)$ and $\frac{\partial\widetilde{n}}{\partial\eta}(\xi,\eta)$ are 0-mean random variables with variance:

$$\mathrm{Var}\left(\frac{\partial\widetilde{n}}{\partial\cdot}(\xi,\eta)\right)=\frac{v\Delta_x\Delta_y}{16\pi\sigma^4|\Psi(\xi,\eta,0)|^2} \tag{107}$$

We do not detail for the sake of brevity, but with the same techniques as above, it is possible to derive:

$$\begin{aligned}\mathrm{Covar}\left(\frac{\partial\widetilde{n}}{\partial\xi}(\xi,\eta),\frac{\partial\widetilde{n}}{\partial\xi}(\xi',\eta')\right) =& \frac{v\Delta_x\Delta_y}{16\pi\sigma^4}e^{-(\xi-\xi')^2/(4\sigma^2)-(\eta-\eta')^2/(4\sigma^2)}\\ &\cdot\frac{\cos(\phi_1(\xi,\eta)-\phi_1(\xi',\eta'))}{|\Psi(\xi,\eta,0)||\Psi(\xi',\eta',0)|}\left(1-\frac{(\xi-\xi')^2}{2\sigma^2}\right)\end{aligned} \tag{108}$$

and:

$$\begin{aligned}\mathrm{Covar}\left(\frac{\partial\widetilde{n}}{\partial\eta}(\xi,\eta),\frac{\partial\widetilde{n}}{\partial\eta}(\xi',\eta')\right) =& \frac{v\Delta_x\Delta_y}{16\pi\sigma^4}e^{-(\xi-\xi')^2/(4\sigma^2)-(\eta-\eta')^2/(4\sigma^2)}\\ &\cdot\frac{\cos(\phi_1(\xi,\eta)-\phi_1(\xi',\eta'))}{|\Psi(\xi,\eta,0)||\Psi(\xi',\eta',0)|}\left(1-\frac{(\eta-\eta')^2}{2\sigma^2}\right)\end{aligned} \tag{109}$$

Assuming as above that the phase variations are locally limited, these covariances reduce into:

$$\begin{aligned}\mathrm{Covar}\left(\frac{\partial\widetilde{n}}{\partial\xi}(\xi,\eta),\frac{\partial\widetilde{n}}{\partial\xi}(\xi',\eta')\right) =& \frac{v\Delta_x\Delta_y}{16\pi\sigma^4|\Psi(\xi,\eta,0)||\Psi(\xi',\eta',0)|}\\ &\cdot e^{-(\xi-\xi')^2/(4\sigma^2)-(\eta-\eta')^2/(4\sigma^2)}\left(1-\frac{(\xi-\xi')^2}{2\sigma^2}\right)\end{aligned} \tag{110}$$

and:

$$\begin{aligned}\mathrm{Covar}\left(\frac{\partial\widetilde{n}}{\partial\eta}(\xi,\eta),\frac{\partial\widetilde{n}}{\partial\eta}(\xi',\eta')\right) =& \frac{v\Delta_x\Delta_y}{16\pi\sigma^4|\Psi(\xi,\eta,0)||\Psi(\xi',\eta',0)|}\\ &\cdot e^{-(\xi-\xi')^2/(4\sigma^2)-(\eta-\eta')^2/(4\sigma^2)}\left(1-\frac{(\eta-\eta')^2}{2\sigma^2}\right)\end{aligned} \tag{111}$$

Consequently, if Ψ can be considered as a constant, then the noise derivatives are wide-sense stationary processes (the autocovariances only depend on $\xi - \xi'$ and $\eta - \eta'$.) As expected (see e.g. [1]), we get the opposite of the second-order derivatives with respect to ξ or η of the autocovariance function of the process $\widetilde{n}$, given by eq. (102).

This result means that the variance of the noise in the phase derivative has been divided by $2\sigma^2$ compared to the noise in the phase itself. The intuition behind is that a large σ yields long-range spatial autocorrelation, thus a smoother noise process.

Let us sum up. Under the same assumptions as in section 3.2.1, the noise on the phase map derivatives is a stationary 0-mean Gaussian process with variance given by eq. (107) and autocovariances by eq. (110) and (111).

3.2.3 Estimating $|\Psi(\xi, \eta, 0)|$

From eq. (97) and (107) we can see that $|\Psi(\xi, \eta, 0)|$ can be seen as an indicator of the confidence in the phase map ϕ_1 and its derivatives. The smaller $|\Psi(\xi, \eta, 0)|$, the larger the noise variance and the uncertainty on the phase and the derivatives. In addition, the Taylor series expansion (eq (94)) is valid assuming that the noise variance is small with respect to $|\Psi(\xi, \eta, 0)|$. Besides, considering $|\Psi|$ as a constant yield stationary noise. We give here a heuristic derivation of an approximation of $|\Psi|$. Under the assumption of section 2.2 (cf Approximation 1), we can write $|\Psi(\xi, \eta, 0)| \simeq |d_1|\gamma A/2 \left|\iint g_\sigma(x-\xi, y-\eta)e^{i\phi_1(x,y)} \, \mathrm{d}x \, \mathrm{d}y\right|$. Now, from lemma 2.4 in section 2.3.2:

$$\begin{aligned} |\Psi(\xi, \eta, 0)| &\simeq |d_1|\frac{\gamma A}{2} \iint g_\sigma(x-\xi, y-\eta)\cos(\phi_1(x,y) - \alpha_\sigma(\xi,\eta)) \, \mathrm{d}x \, \mathrm{d}y && (112) \\ &\simeq |d_1|\frac{\gamma A}{2} - |d_1|\frac{\gamma A}{4} \cdot \iint g_\sigma(x-\xi, y-\eta)(\phi_1(x,y) - \alpha_\sigma(\xi,\eta))^2 \, \mathrm{d}x \, \mathrm{d}y && (113) \end{aligned}$$

The latter equation holds using a Taylor expansion of cos inside the analysis window and because g_σ integrates to 1. Developing the rightmost term yields:

$$\begin{aligned} \iint g_\sigma(x-\xi, y-\eta)(\phi_1(x,y) - \alpha_\sigma(\xi,\eta))^2 \, \mathrm{d}x \, \mathrm{d}y &= g_\sigma * \phi_1^2(\xi,\eta) - 2\alpha_\sigma(\xi,\eta) \cdot g_\sigma * \phi_1(\xi,\eta) + \alpha_\sigma(\xi,\eta)^2 \\ &= g_\sigma * \phi_1^2(\xi,\eta) - (g_\sigma * \phi_1(\xi,\eta))^2 \end{aligned} \tag{114}$$

since $\alpha_\sigma \simeq g_\sigma * \phi$ and g_σ integrates to 1.

Plugging a Taylor series approximation of ϕ_1 inside the window g_σ centered at (ξ, η) (i.e. $\phi_1(x,y) \simeq \phi_1(\xi,\eta) + (x-\xi, y-\eta)\nabla\phi_1(\xi,\eta)$) in the right-hand part of eq. (114):

$$\begin{aligned} &\iint g_\sigma(x-\xi, y-\eta)(\phi_1(x,y) - \alpha_\sigma(\xi,\eta))^2 \, \mathrm{d}x \, \mathrm{d}y \simeq \phi_1^2(\xi,\eta) \\ &+ \left((\frac{\partial\phi_1}{\partial\xi})^2 + (\frac{\partial\phi_1}{\partial\eta})^2 \right) \iint x^2 g_\sigma + 2\phi_1(\frac{\partial\phi_1}{\partial\xi} + \frac{\partial\phi_1}{\partial\eta}) \iint x g_\sigma + 2\frac{\partial\phi_1}{\partial\xi}\frac{\partial\phi_1}{\partial\eta} \iint xy g_\sigma \\ &- \left(\phi_1(\xi,\eta) + \left(\frac{\partial\phi_1}{\partial\xi} + \frac{\partial\phi_1}{\partial\eta} \right) \iint x g_\sigma \right)^2 \end{aligned} \tag{115}$$

Since $\iint xy g_\sigma = \iint x g_\sigma = 0$ and $\iint x^2 g_\sigma = \sigma^2$, this simplifies into:

$$\iint g_\sigma(x-\xi, y-\eta)(\phi_1(x,y) - \alpha_\sigma(\xi,\eta))^2 \, \mathrm{d}x \, \mathrm{d}y \simeq \sigma^2 ||\nabla\phi_1||_2^2 \tag{116}$$

From this heuristic reasoning, which we will support with numerical assessments, we conclude that $|\Psi(\xi,\eta,0)|$ can be approximated by:

$$|\Psi(\xi,\eta,0)| \simeq |d_1|\frac{\gamma A}{2}\left(1-\frac{\sigma^2}{2}||\nabla\phi_1||_2^2\right) \tag{117}$$

The conclusion of this discussion is that the noise and the noise on the phase derivative is amplified where the gradient of the phase has large values, which correspond to regions of interest in the strain field. However, in practice the gradient of the phase is small enough so that $\sigma||\nabla\phi_1||_2 \simeq 0$ (typical values are $\sigma \simeq 5$ pixels and $\nabla\phi_1 \simeq 10^{-3}$ pixel^{-1}), and $|\Psi|$ can actually be considered as a constant, equal to $|d_1|\frac{\gamma A}{2}$. It does not depends on θ, hence in this case $|\Psi(\xi,\eta,0| = |\Psi(\xi,\eta,\pi/2|$. Remark that this constant is all the larger as the lighting A and the contrast γ of the lines are strong. This is consistent with the intuition: in this case the signal-to-noise ratio is larger and measurement uncertainty is smaller.

Let us point out that the link between the phase and the modulus in windowed Fourier transform is discussed in a very recent paper [3]. Our study is different in that we look at the 2D windowed Fourier transform at a given frequency pair (either $(f,0)$ or $(0,f)$.) For low contrasted images or large $\sigma||\nabla\phi||$ (in other frameworks), the modulus can be locally near zero. Let us also point out that the phase behaviour when the modulus is almost 0 in the (1D) windowed Fourier transform has been characterized in [3, 7, 13].

3.2.4 The $d_1 = 0$ case

It is possible that frng is a 2π-periodic function with $d_1 = 0$. However, the whole framework would still hold with any lf analysis frequency ($l \in \mathbb{Z}^*$), yielding in particular:

$$\text{angle}\left(\iint s(x,y)g_\sigma(x-\xi,y-\eta)e^{-2i\pi lfx}\,\mathrm{d}x\,\mathrm{d}y\right) \simeq \text{angle}(d_l) + g_\sigma * \phi_1(\xi,\eta) \tag{118}$$

In principle, we can estimate the phases and the derivatives with any l such that $d_l \neq 0$. Nevertheless, section 3.2.3 indicates that the noise is weaker if d_l is larger, which in most cases happens for $l = 1$.

4 Numerical assessment

We use synthetic yet realistic phase maps ϕ_1 and ϕ_2 in order to assess that the approximated estimates of sections 2 and 3 are valid.

Figure 2 shows two synthetic phases ϕ_1 and ϕ_2 and phase derivatives $\partial\phi_1/\partial\xi$ and $\partial\phi_2/\partial\eta$. The phase ϕ_1 has a triangle profile (slope=1 on 50 pixels, then slope=-1 on 50 pixels) along the ξ axis. Its derivative along η axis is thus zero, and along ξ axis is a 1 / -1 step function. The phase ϕ_2 is a sine along η-axis, whose period slowly and linearly varies as a function of ξ. Both phases are normalized in such a way that the largest value of their derivative, denoted m, is controlled. A realistic value for our problem is $m = 0.001$ pixel^{-1}. Note that while ϕ_2 is smooth, ϕ_1 is not.

Note that ϕ_1 and ϕ_2 are defined independently. Hence they do not satisfy the compatibility equations [2]. However, these additional constraints are not covered by our work. The phase maps are chosen here only for didactic and illustrative purposes.

From these synthetic phases we create a grid image which satisfies the formulation of eq. (1) ($A = 2^{11}$ and $\gamma = 1$):

$$u(x,y) = 2^{11} + 2^{10}\sin^3\left(\frac{2\pi}{5}(x-1)+\phi_1(x,y)\right) + 2^{10}\sin^3\left(\frac{2\pi}{5}(y-1)+\phi_2(x,y)\right) + n(x,y) \tag{119}$$

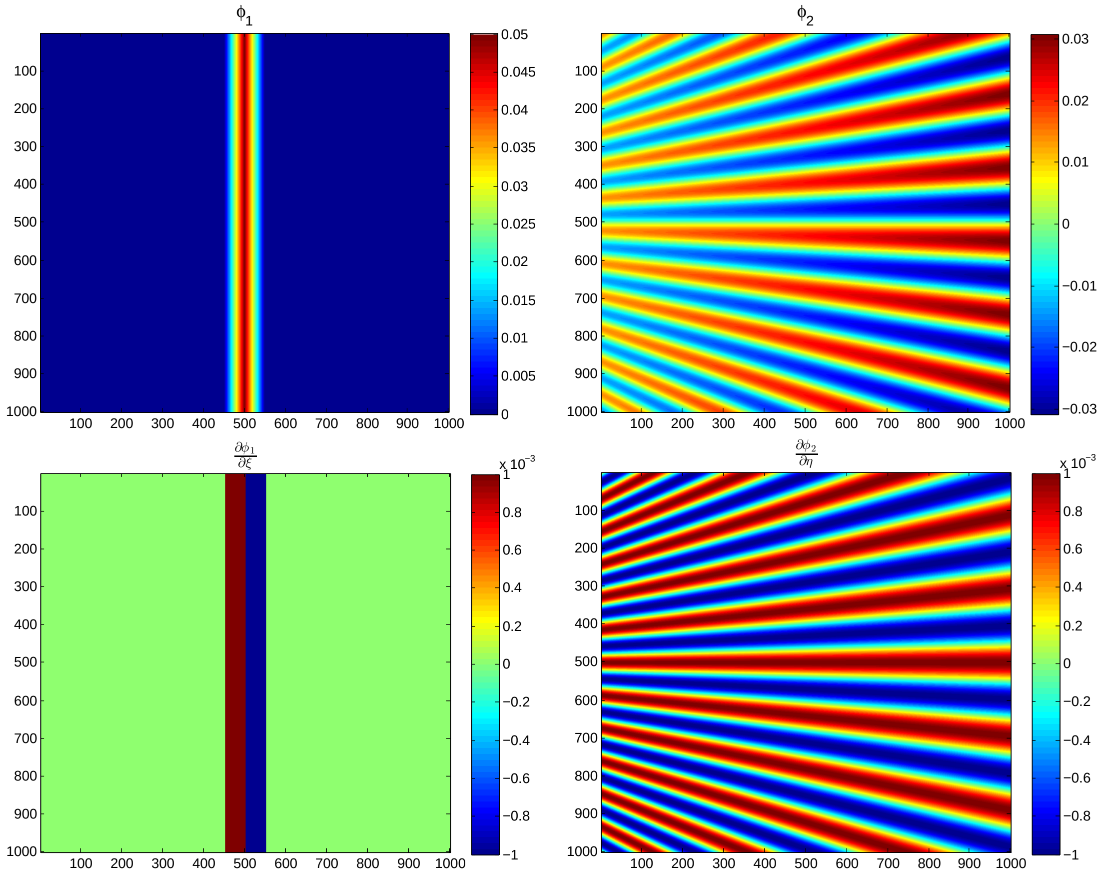

Figure 2: Top: the synthetic phases ϕ_1 (on the left) and ϕ_2 (on the right.) Bottom: the derivatives $\partial\phi_1/\partial\xi$ (on the left) and $\partial\phi_2/\partial\eta$ (on the right.) The amplitude m of the partial derivatives is set here to 0.001 pixel^{-1}.

for (x,y) spanning the range $\{1\dots X\}\times\{1\dots Y\}$ (here $X=Y=1,000$ pixels), where n is a Gaussian white noise with variance v. With the Sensicam-QE one camera, $\sqrt{v}=2$ is a realistic value (the manufacturer claims that SNR > 70 db). We have chosen to model $\mathsf{frng}(x)$ by $\sin^3(x)$ to simulate realistic sharp grid lines. Gray-scale is then quantized over 12 bits as in this camera. Here the inter-line distance is $p=1/f=5$ pixels.

4.1 Assessment of approximations 2 and 3 in section 2.2

Computing the phase of $\Psi(x,y,0)$ and $\Psi(x,y,\pi/2)$ gives an estimate of the phases ϕ_1 and ϕ_2 with Approximation 2 (eq. (39) and (40).) Since we have here an analytic expression of the function frng, we can compute d_1:

$$d_1=\frac{1}{2\pi}\int_0^{2\pi}\sin(x)^3e^{-ix}\,\mathrm{d}x=\frac{1}{-16\pi i}\int_0^{2\pi}\left(e^{ix}-e^{-ix}\right)^3e^{-ix}\,\mathrm{d}x=\frac{1}{-16\pi i}\times(-6\pi)=-3/8i \tag{120}$$

As a consequence angle$(d_1)=-\pi/2$.

We assess the validity of Approximation 2 by computing the Normalized Root Mean Square Error (NRMSE), i.e. the RMSE between the phase map retrieved by the windowed Fourier transform and the actual phase map (perfectly known in the present synthetic case) convolved by the analysis window, normalized by the maximum value of the convolved phase map:

$$\text{NRMSE}\left(\alpha_\sigma(\phi.)+\frac{\pi}{2},g_\sigma*\phi.\right)=\frac{\sqrt{\frac{1}{XY}\sum_{\xi,\eta}\left|\alpha_\sigma(\phi.)+\frac{\pi}{2}-g_\sigma*\phi.(\xi,\eta)\right|^2}}{\max_{\xi,\eta}g_\sigma*\phi.(\xi,\eta)} \tag{121}$$

where $\alpha_\sigma(\phi_1)$ denotes the phase of $\Psi(\xi,\eta,0)$ and $\alpha_\sigma(\phi_2)$ denotes the phase of $\Psi(\xi,\eta,\pi/2)$.

Concerning the assessment of approximation 3 (eq. (42) to (45)) which deals with phase derivatives instead of phases, we compute in a similar manner NRMSE $\left(\frac{\partial\alpha_\sigma(\phi.)}{\partial\cdot},g_\sigma*\frac{\partial\phi.}{\partial\cdot}\right)$.

Figure 3 shows how the NRMSE evolves when σ increases, for various values of the standard deviation $\sqrt{v}$ of the image noise. We can see that the NRMSE in approximating $\alpha_\sigma(\phi)$ by $g_\sigma*\phi$ is less than 0.1% as soon as the window size σ is large enough with respect to the noise level. Larger noise level needs larger σ to attain a given NRMSE. This is consistent with the discussion in section 3: larger σ are more efficient at smoothing out the noise from the phase maps. Concerning the phase derivatives, it can be noted that the NRMSE in approximating the derivatives of $\alpha_\sigma(\phi)$ by $g_\sigma*(\partial\phi/\partial\cdot)$ is this time around 1%. Compared to the phase maps, smaller σ are needed to smooth out the noise at a given NRMSE. This is consistent with eq. (107), where the noise variance in the phase derivative maps is divided by σ^4, while eq. (89) shows that noise variance in the phase maps is only divided by σ^2.

This experiment shows that, practically speaking, Approximation 2 and 3 are tight up to less than 1%.

Figure 4 shows the retrieved phase and its derivative for several values of σ. We have represented cross-sections of ϕ_1 and $\partial\phi_1/\partial\xi$ at $\eta=500$, and cross-sections of ϕ_2 and $\partial\phi_2/\partial\eta$ at $\xi=500$. They actually look like the convolution of the Gaussian window with the true phase and phase derivatives (illustrated in figure 2).

4.2 Assessing the classic estimation of the phase and phase derivative

We also assess the quality of the classic estimation of ϕ_1 and ϕ_2, when they are simply approximated by the phase α_σ of $\Psi(\xi,\eta,\cdot)$, and the phase derivatives by the derivatives of α_σ [17, 5, 6].

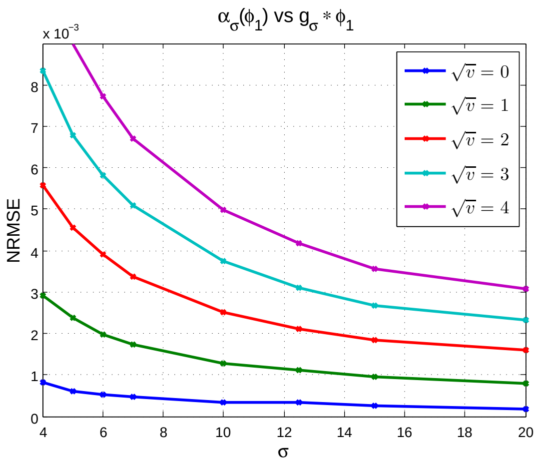

a) NRMSE between $\alpha_\sigma(\phi_1)$ and $g_\sigma * \phi_1$

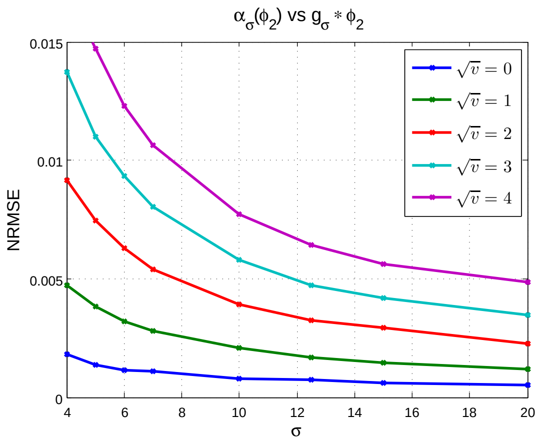

b) NRMSE between $\alpha_\sigma(\phi_2)$ and $g_\sigma * \phi_2$

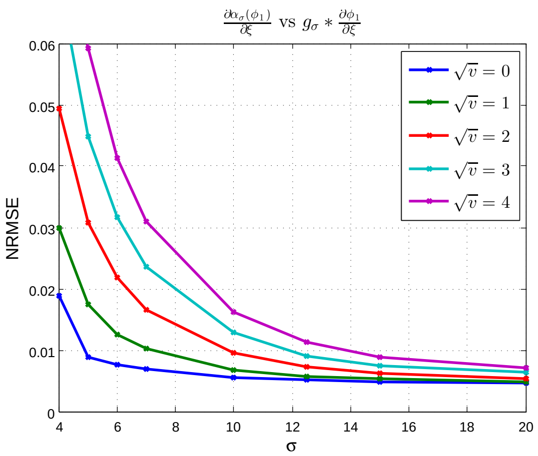

c) NRMSE between $\partial \alpha_\sigma(\phi_1)/\partial \xi$ and $g_\sigma * (\partial \phi_1/\partial \xi)$

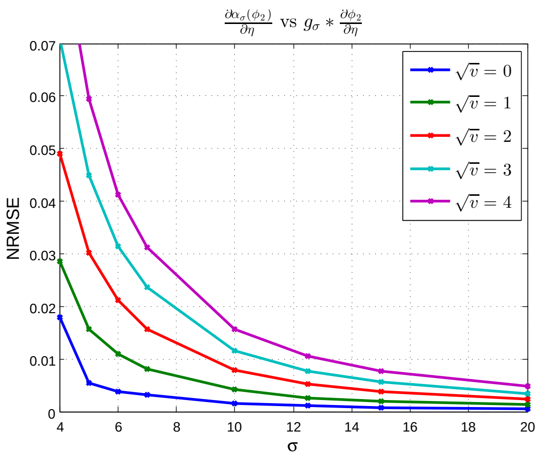

d) NRMSE between $\partial \alpha_\sigma(\phi_2)/\partial \eta$ and $g_\sigma * (\partial \phi_2/\partial \eta)$

Figure 3: Assessing approximations 2 and 3 with $m = 0.001$ pixel^{-1}.

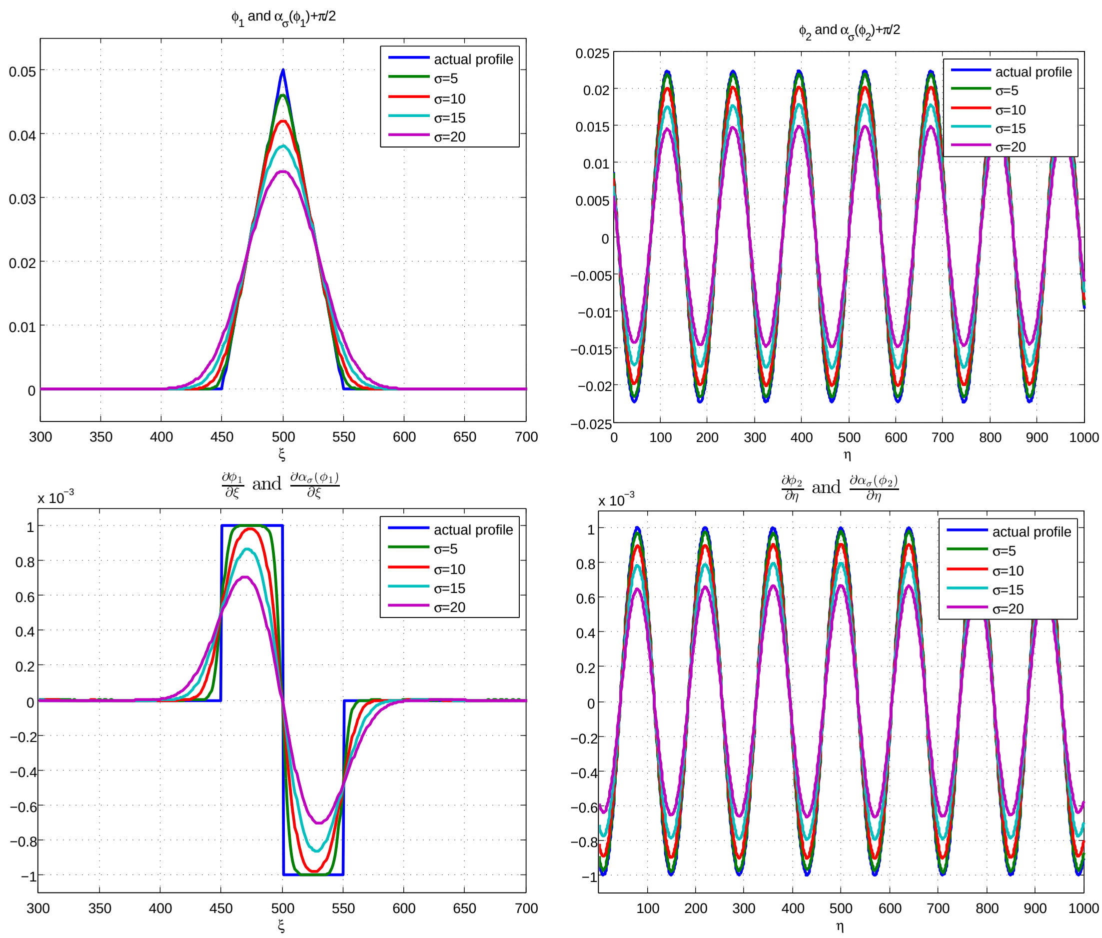

Figure 4: Behavior of the retrieved phase and phase derivative maps with respect to σ, illustrated on a cross-section.

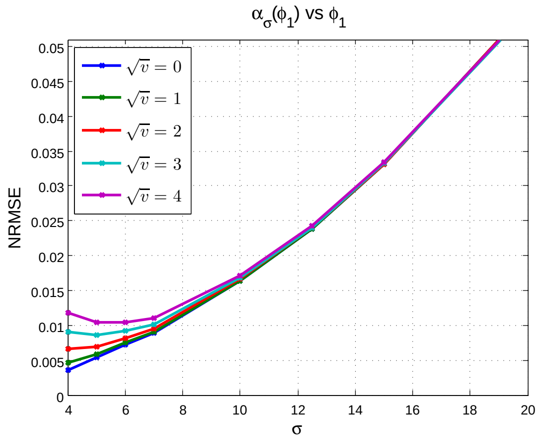

a) NRMSE between $\alpha_\sigma(\phi_1)$ and ϕ_1

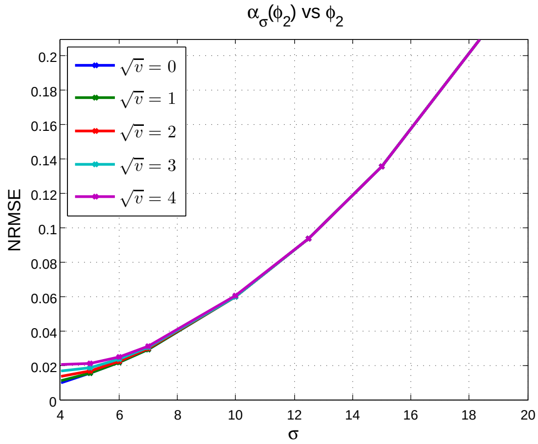

b) NRMSE between $\alpha_\sigma(\phi_2)$ and ϕ_2

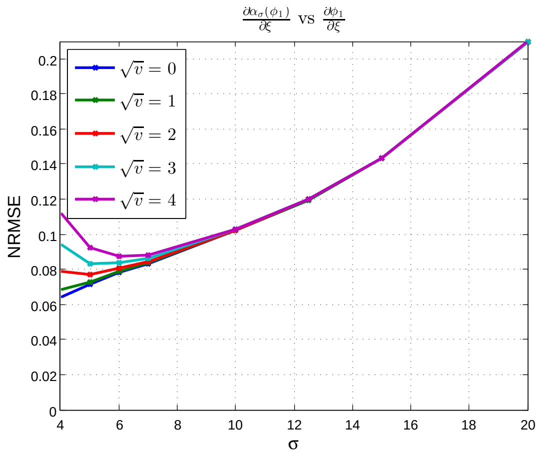

c) NRMSE between $\partial\alpha_\sigma(\phi_1)/\partial\xi$ and $\partial\phi_1/\partial\xi$

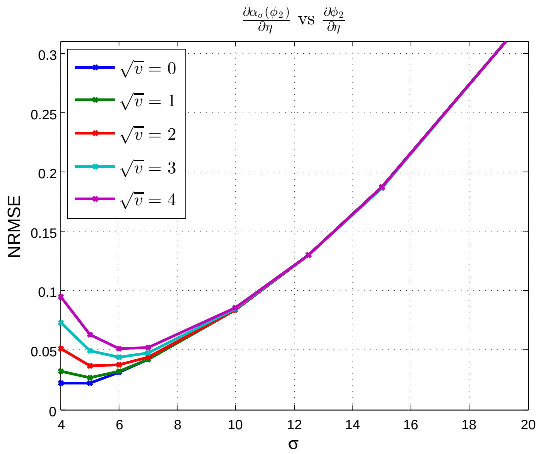

d) NRMSE between $\partial\alpha_\sigma(\phi_2)/\partial\eta$ and $\partial\phi_2/\partial\eta$

Figure 5: Assessing the classic approach with $m = 0.001$ pixel^{-1}.

Figures 5 shows the variations of NRMSE $\left(\alpha_\sigma(\phi.) + \frac{\pi}{2}, \phi.\right)$ and NRMSE $\left(\frac{\partial\alpha_\sigma(\phi.)}{\partial\cdot}, \frac{\partial\phi.}{\partial\cdot}\right)$ with respect to σ, for several values of $\sqrt{v}$. We can see that for moderate values of σ, estimating ϕ with $\alpha_\sigma(\phi)$ gives an NRMSE around 1 to 5%, and estimating the phase derivatives with the derivatives of α_σ gives an NRMSE around 5 to 10%. The estimates with the classic method (the procedure proposed in [5, 6] was used in practice) thus give results close to the reference value when no noise corrupts the grid image. In [11], we will show that the tighter approximations derived in the present report permit to build deconvolution algorithms that outperform the classic estimate.

In addition, note that the larger σ, the larger the deviation from the actual value. In this method, a trade-off must be met between the accuracy of the estimation of the phase and its derivatives and the smoothing needed by the image noise.

4.3 Assessing the properties of the windowed Fourier transform of a Gaussian white noise (section 3.1)

As a sanity check, we assess on two cases the validity of propositions 3.1 and 3.2 of section 3.1. Hence we deliberately choose $f\sigma \leq 1$, contrary to the realistic case. We can see in Fig. 6 that the larger σ, the smaller the variance of $\widehat{n}$ (cf the colorbar range of real and imaginary parts of $\widehat{n}$.) The respective size of the "blobs" in the real and imaginary parts also proves longer range autocovariance. As expected from the theory (eq. (86) to (88), sample variance and covariance exhibit a $1/2f$ periodicity (20 in case a) and 30 in case b)). The variance is supposed to follow a sine spanning the interval

$$[v\Delta_x\Delta_y/(8\pi\sigma^2)\cdot(1-e^{-4\pi^2\sigma^2f^2}),\ v\Delta_x\Delta_y/(8\pi\sigma^2)\cdot(1+e^{-4\pi^2\sigma^2f^2})] \tag{122}$$

(numerically: $[0.0239, 0.8603]$ in a), $[0.095, 0.0398]$ in b)), and autocovariance spans:

$$[-v\Delta_x\Delta_y/(8\pi\sigma^2)\cdot e^{-4\pi^2\sigma^2f^2}, v\Delta_x\Delta_y/(8\pi\sigma^2)\cdot e^{-4\pi^2\sigma^2f^2}] \tag{123}$$

($[-0.4182, 0.4182]$ in a), $[-0.0302, 0.0302]$ in b).)

We can check that these claims are well supported by the graphs of sample variance and covariance, in spite that the approximation of sums by integrals in prop. 3.2 and the limited accuracy of sampling methods prevent from getting a perfect sine.

The average standard deviation of real and imaginary parts of $\widehat{n}$ are theoretically $v\Delta_x\Delta_y/(8\pi\sigma^2)$ (i.e. 0.4421 in a) and 0.0398 in b)); they are actually estimated as 0.4437 for real part of $\widehat{n}$ and 0.4487 for imaginary part in case a), and 0.0377 and 0.0363 for real and imaginary parts in case b).

4.4 Assessing the approximation for $|\Psi|$ (section 3.2.3)

Eq. (117) in section 3.2.3 gives an approximation of $|\Psi(\xi,\eta,\cdot)|$. Figure 7 shows two examples of $|\Psi(\xi,\eta,\cdot)|$ image pairs. In the first example, $m = 10^{-3}$ pixel^{-1} and $\sigma = 20$ pixels. In the second example, $m = 10^{-2}$ pixel^{-1} and $\sigma = 7$ pixels. In both cases, $|d_1|\gamma A/2 = 0.375\times 2^{10} = 384$. In the first case, $\sigma^2m^2/2 = 2\cdot 10^{-4}$ (thus $|\Psi|$ is expected to vary between 384 and 383.92) while in the second case, $\sigma^2m^2/2 = 2.45\cdot 10^{-4}$ (thus $|\Psi|$ is expected to vary between 384 and 383.06.) This is actually the range of the modulus that can be seen in figure 7. The value of $|\Psi|$ is actually approximately constant, equal to $\gamma A/2$.

4.5 Assessing the effect of the image noise on the phase and phase derivative maps (section 3.2.1 and 3.2.2)

We are now within the noisy grid image model. Figure 8 shows the retrieved phases and phase derivatives for $\sigma = 5$ pixels and $\sigma = 10$ pixels, when $m = 0.001$ pixel^{-1} and $\sqrt{v} = 5$. We can see that this creates "blob"-like structures in the phase and phase derivatives, which are due to the spatial autocorrelation of the noise $\widehat{n}$. As announced by section 3.2.2, the phase derivatives along the ξ- and η-directions are affected by a noise correlated in these directions (specially visible when $\sigma = 5$ pixels.) Increasing σ to 10 pixels permits to visually smooth out the noise in the phase and phase derivative maps.

We also assess the validity of the autocovariances estimated in sections 3.2.1 and 3.2.2, with a Monte-Carlo simulation. Here we take $5,000$ runs. Figure 9 shows the sample autocovariance functions of the phase noise and of the phase derivative noise, at four randomly chosen (ξ,η). We have used different sets of parameters v, σ, m. In all cases, the NRMSE between the sample autocovariance function and the theoretic function was below 0.5%.

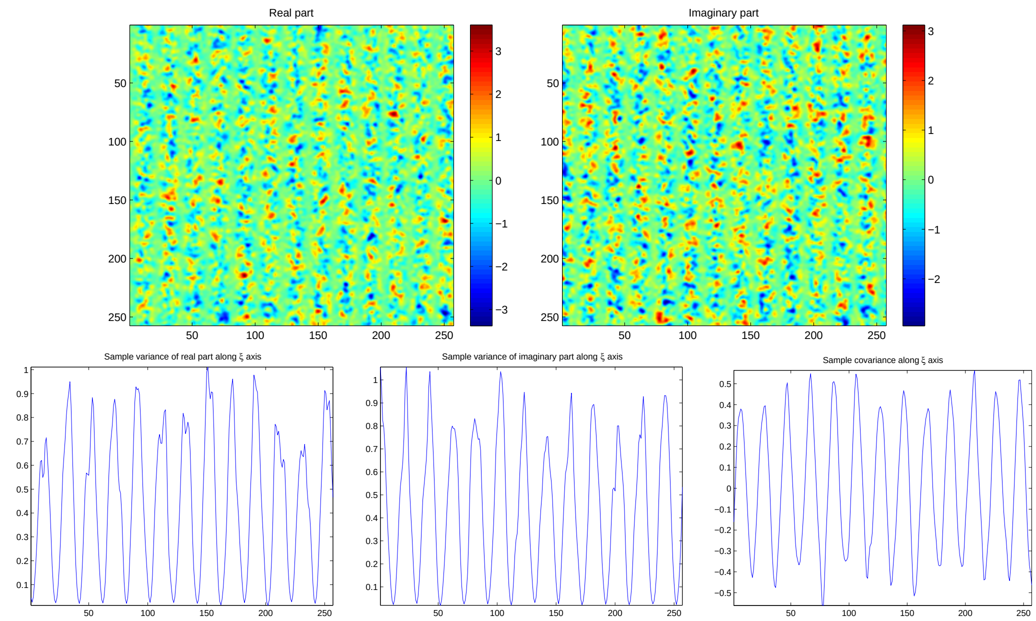

a) $\sqrt{v} = 5$, $\sigma = 1.5$ pixel, $f = 1/40$ pixel^{-1}

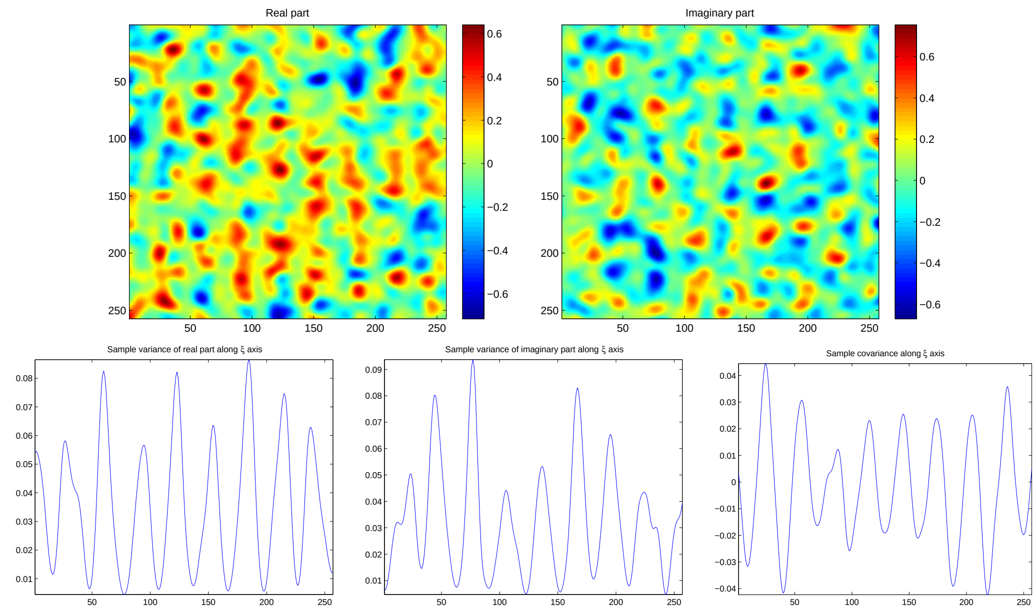

b) $\sqrt{v} = 5$, $\sigma = 5$ pixels, $f = 1/60$ pixel^{-1}

Figure 6: Windowed Fourier transform of a Gaussian white noise. Here are shown for two cases a) and b) the real and imaginary parts of $\widehat{n}$, then the sample variance of $\mathrm{Re}(\widehat{n}(\xi, \eta)$ and of $\mathrm{Im}(\widehat{n}(\xi, \eta)$ along ξ-axis, and the sample covariance between $\mathrm{Re}(\widehat{n}(\xi, \eta)$ and $\mathrm{Im}(\widehat{n}(\xi, \eta)$ along ξ-axis (each of these estimators is obtained by summation over the η-axis.)

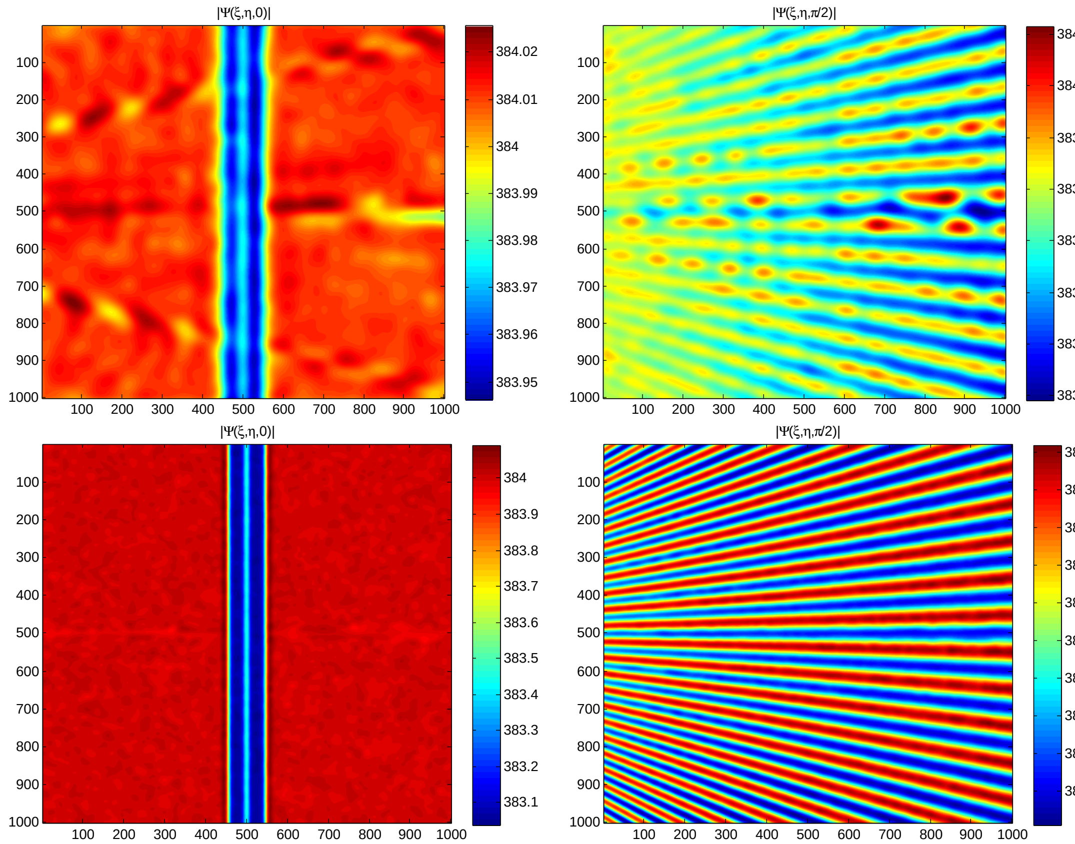

Figure 7: Illustrating $|\Psi(x, y, 0)|$ (on the left) and $|\Psi(x, y, \pi/2)|$ (on the right.) Top: $m = 10^{-3}$ pixel^{-1}, $\sigma = 20$ pixels. Bottom: $m = 10^{-2}$ pixel^{-1}, $\sigma = 7$ pixels. The value of $|\Psi|$ is actually approximately constant, and behaves as predicted by equation 117, apart from some artifacts.

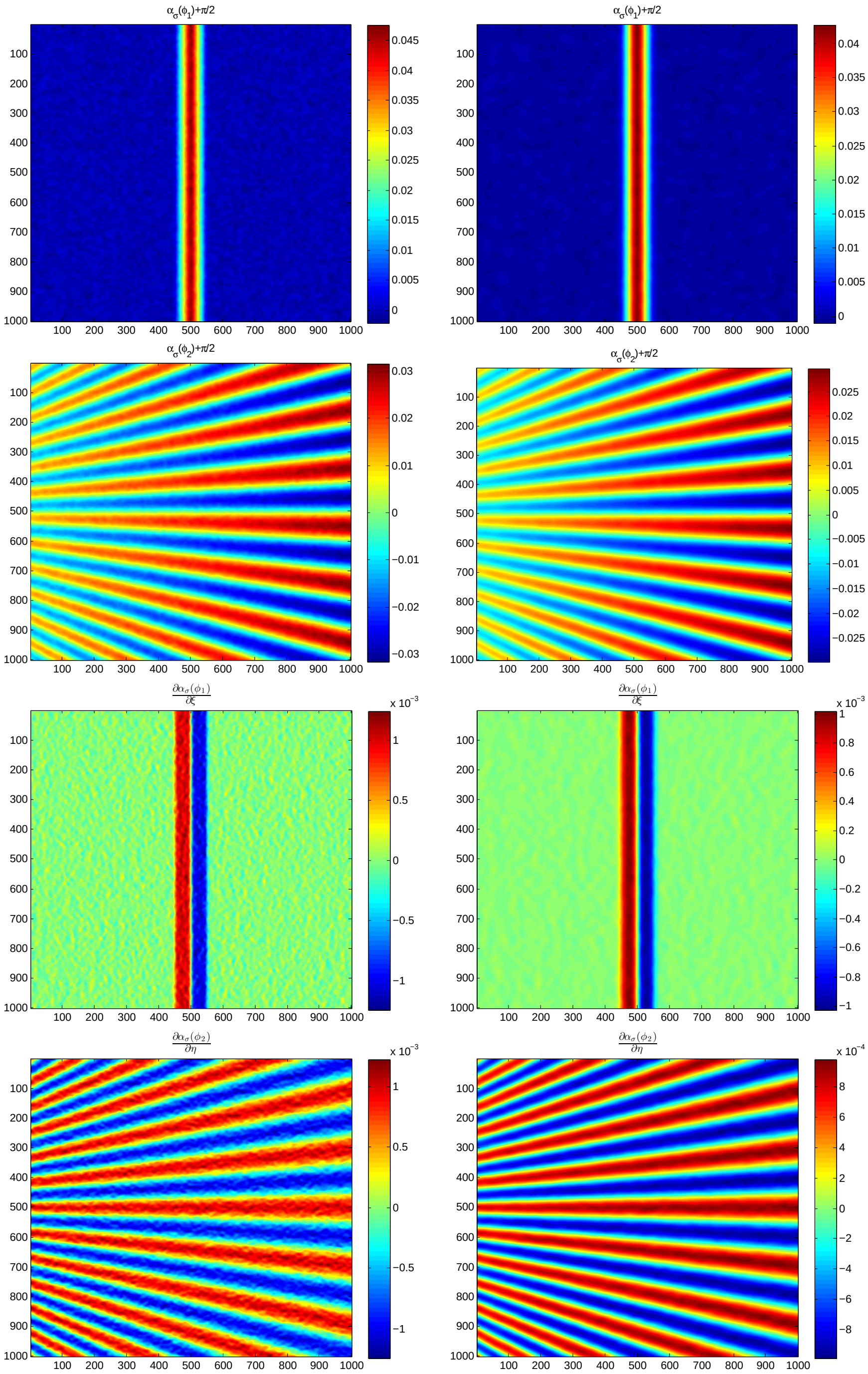

Figure 8: Illustrating how a Gaussian white noise on the grid image transfers to the retrieved phase and phase derivative maps. From top to bottom: $\alpha_\sigma(\phi_1)$, $\alpha_\sigma(\phi_2)$, $\partial\alpha_\sigma(\phi_1)/\partial\xi$, $\partial\alpha_\sigma(\phi_2)/\partial\eta$. On the left: $\sigma = 5$ pixels. On the right: $\sigma = 10$ pixels. In both case $m = 0.001$ pixel^{-1} and $\sqrt{v} = 5$.

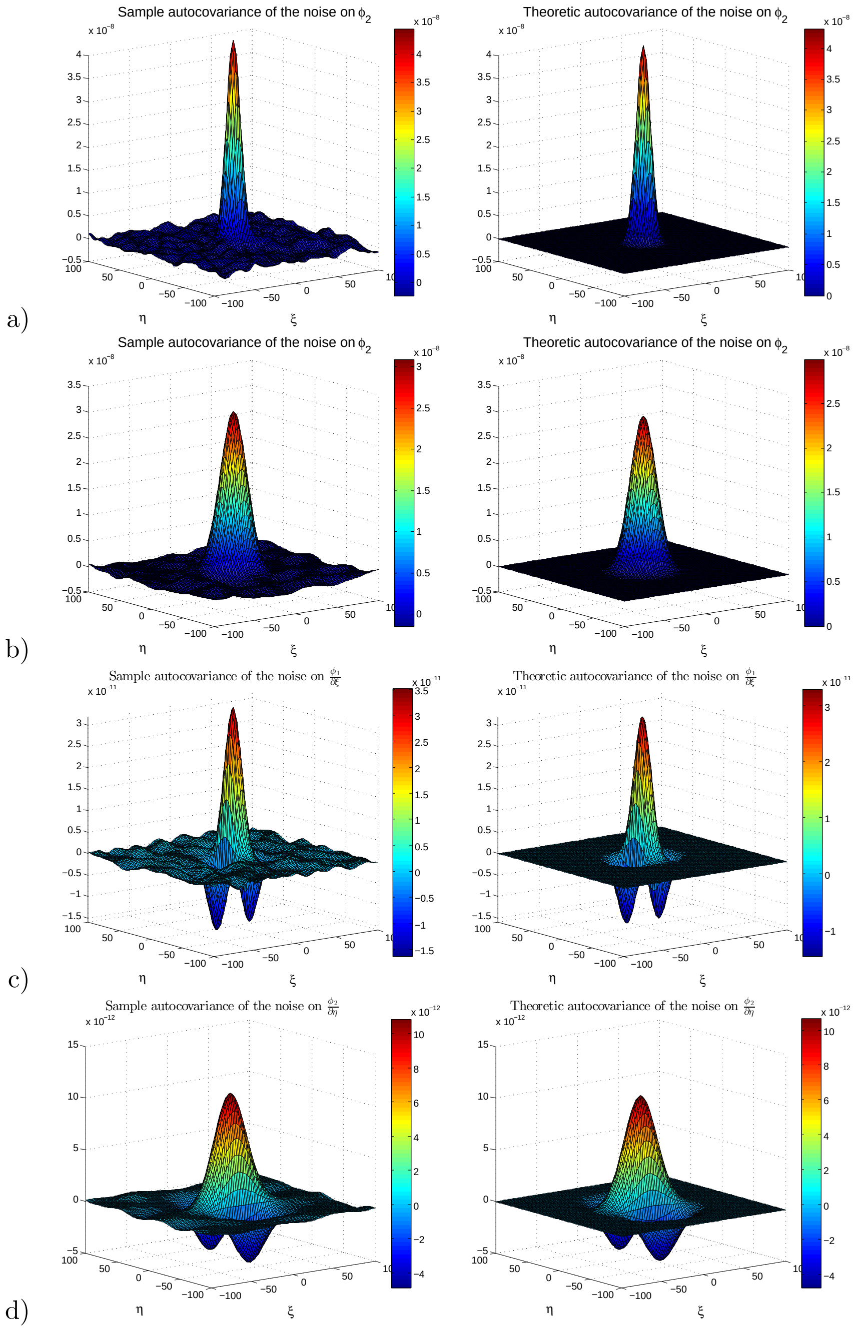

Figure 9: Assessing the estimation of the noise on the phase maps and on the phase derivatives with Monte-Carlo simulation. On the left: sample autocovariance. On the right: theoretical autocovariance (see sections 3.2.1 and 3.2.2). a) noise on ϕ_1, $\sqrt{v} = 2$, $\sigma = 5$ pixels, $m = 0.01$ pixel^{-1}, b) noise on ϕ_2, $\sqrt{v} = 3$, $\sigma = 9$ pixels, $m = 0.0001$ pixel^{-1}, c) noise on $\partial\phi_1/\partial\xi$, $\sqrt{v} = 1$, $\sigma = 8$ pixels, $m = 0.001$ pixel^{-1}, d) noise on $\partial\phi_2/\partial\eta$, $\sqrt{v} = 1.5$, $\sigma = 13$ pixels, $m = 0.001$ pixel^{-1}.

5 Conclusion

This report is about the grid method for in-plane measurements, within the windowed Fourier analysis framework. In this study we have first shown that the phases or the derivatives are approximately the result of the convolution of the actual phases or derivatives and the window function (Approximation 2, eq. (39-40) and Approximation 3, eq. (42-45) in section 2.) The second contribution is the characterization of the noise on the phase maps and the derivatives (autocovariances in eq. (102) and (110-111), variances in eq. (97) and (107), respectively, in section 3.) In a dedicated report [11], we discuss restoration techniques based on the present theoretical study. The crucial point is that the convolution function has been perfectly characterized, contrary to most cases in the image processing literature. We are therefore within non-blind image deconvolution. It turns out that the accurate estimate of the noise on the phases and on the derivatives is crucial for restoration, as illustrated in the companion report [11].

A Some useful basic results

To make the report easier to read, we recall some basic results.

Proposition A.1 *Fourier transform of a translated function:*

$$\iint f(x-\xi, y-\eta)e^{-2i\pi(x\alpha+y\beta)}\ dx\ dy = \widehat{f}(\alpha,\beta)e^{-2i\pi(\xi\alpha+\eta\beta)} \tag{124}$$

Proposition A.2 *Let X and X' be two independent Gaussian random variable (respective mean m and m', variance v and v'). Then $aX+a'X'$ is a Gaussian random variable of mean $am+a'm'$ and variance $a^2v+a'^2v'$.*

Proposition A.3 *(Taylor's theorem.) Let $f:\mathbb{R}^2\to\mathbb{R}$ be a C^2 function on $B((a,b),r)$ (that is, the open ball centered at (a,b) of radius $r>0$). Then, for any $(x,y)\in B((a,b),r)$ there exists δ belonging to the line segment connecting $[a,b]$ to $[x,y]$ such that:*

$$f(x,y) = f(a,b)+(x-a,y-b)\,\nabla f(a,b)\,(x-a,y-b)^T+\frac{1}{2}(x-a,y-b)H(\delta)(x-a,y-b)^T \tag{125}$$

B Computations for proposition 3.1

Proposition B.1

$$\iint e^{-\frac{x^2+y^2}{\sigma^2}}\ dx\ dy = \pi\sigma^2 \tag{126}$$

$$\iint e^{2i\pi(\alpha x+\beta)}e^{-\frac{x^2+y^2}{\sigma^2}}\ dx\ dy = \pi\sigma^2e^{-\pi^2\sigma^2\alpha^2+2\pi i\beta} \tag{127}$$

Proof. For the first equality:

$$\iint e^{-\frac{x^2+y^2}{\sigma^2}}\ \mathrm{d}x\ \mathrm{d}y = \pi\sigma^2\iint g_\sigma(x,y)\ \mathrm{d}x\ \mathrm{d}y$$

by the changes of variables $x \leftarrow x/\sqrt{2}$ and $y \leftarrow y/\sqrt{2}$; and g_σ integrates to 1.

For the second equality:

$$\begin{aligned}\iint e^{2i\pi(\alpha x+\beta)} e^{-\frac{x^2+y^2}{\sigma^2}}\,\mathrm{d}x\,\mathrm{d}y &= \pi\sigma^2 e^{2\pi i\beta} \iint g_\sigma(x,y) e^{i\alpha x/\sqrt{2}}\,\mathrm{d}x\,\mathrm{d}y \\ &= \pi\sigma^2 e^{2\pi i\beta}\widehat{g_\sigma}\left(-\alpha/\sqrt{2}, 0\right) \\ &= \pi\sigma^2 e^{2\pi i\beta} e^{-\pi^2\sigma^2\alpha^2}\end{aligned}$$

since $\widehat{g_\sigma}(\xi,\eta) = e^{-2\pi^2\sigma^2(\xi^2+\eta^2)}$. □

Proposition B.2

$$\iint g_\sigma(x-\xi, y-\eta) g_\sigma(x-\xi', y-\eta') \cos^2(2\pi f x)\; dx\; dy = \frac{1}{8\pi\sigma^2} e^{-\frac{(\xi-\xi')^2+(\eta-\eta')^2}{4\sigma^2}} \cdot \left(1 + e^{-4\pi^2\sigma^2 f^2}\cos(2\pi f(\xi+\xi'))\right) \tag{128}$$

$$\iint g_\sigma(x-\xi, y-\eta) g_\sigma(x-\xi', y-\eta') \sin^2(2\pi f x)\; dx\; dy = \frac{1}{8\pi\sigma^2} e^{-\frac{(\xi-\xi')^2+(\eta-\eta')^2}{4\sigma^2}} \cdot \left(1 - e^{-4\pi^2\sigma^2 f^2}\cos(2\pi f(\xi+\xi'))\right) \tag{129}$$

$$\iint g_\sigma(x-\xi, y-\eta) g_\sigma(x-\xi', y-\eta') \sin(2\pi f x)\cos(2\pi f x)\; dx\; dy = \frac{1}{8\pi\sigma^2} e^{-\frac{(\xi-\xi')^2+(\eta-\eta')^2}{4\sigma^2}} \cdot \sin(2\pi f(\xi+\xi')) e^{-4\pi^2\sigma^2 f^2} \tag{130}$$

Proof. For the first equality:

$$\begin{aligned}&\iint g_\sigma(x-\xi, y-\eta) g_\sigma(x-\xi', y-\eta') \cos^2(2\pi f x)\,\mathrm{d}x\,\mathrm{d}y \\ &= \frac{1}{4\pi^2\sigma^4} \iint e^{-\frac{(x-\xi)^2+(x-\xi')^2+(y-\eta)^2+(y-\eta')^2}{2\sigma^2}} \cdot \frac{1+\cos(4\pi f x)}{2}\,\mathrm{d}x\,\mathrm{d}y \\ &= \frac{1}{8\pi^2\sigma^4} e^{-\left((\xi-\xi')^2+(\eta-\eta')^2\right)/(4\sigma^2)} \iint e^{-\left((x-\frac{\xi+\xi'}{2})^2+(y-\frac{\eta+\eta'}{2})^2\right)/\sigma^2} \left(1+\cos(4\pi f x)\right)\,\mathrm{d}x\,\mathrm{d}y \\ &= \frac{1}{8\pi^2\sigma^4} e^{-\frac{(\xi-\xi')^2+(\eta-\eta')^2}{4\sigma^2}} \iint e^{-(x^2+y^2)/\sigma^2} \left(1+\cos\left(4\pi f\left(x+\frac{\xi+\xi'}{2}\right)\right)\right)\,\mathrm{d}x\,\mathrm{d}y \\ &= \frac{1}{8\pi\sigma^2} e^{-\frac{(\xi-\xi')^2+(\eta-\eta')^2}{4\sigma^2}} \left(1+e^{-4\pi^2\sigma^2 f^2}\cos(2\pi f(\xi+\xi'))\right)\end{aligned}$$

by using eq. (126) in proposition B.1 and by taking the real part in eq. (127) from proposition B.1 with $\alpha = 2f$ and $\beta = f(\xi+\xi')$.

For the second equality:

$$\begin{aligned}&\iint g_\sigma(x-\xi, y-\eta) g_\sigma(x-\xi', y-\eta') \sin^2(2\pi f x)\,\mathrm{d}x\,\mathrm{d}y = \\ &\iint g_\sigma(x-\xi, y-\eta) g_\sigma(x-\xi', y-\eta')\,\mathrm{d}x\,\mathrm{d}y - \iint g_\sigma(x-\xi, y-\eta) g_\sigma(x-\xi', y-\eta') \cos^2(2\pi f x)\,\mathrm{d}x\,\mathrm{d}y \\ &= \frac{1}{8\pi\sigma^2} e^{-\frac{(\xi-\xi')^2+(\eta-\eta')^2}{4\sigma^2}} \left(1-e^{-4\pi^2\sigma^2 f^2}\cos(2\pi f(\xi+\xi'))\right)\end{aligned}$$

(the value of $\iint g_\sigma(x-\xi, y-\eta) g_\sigma(x-\xi', y-\eta') \,\mathrm{d}x \,\mathrm{d}y$ is simply obtained by taking $f = 0$ in eq. (128).)

For the third equality:

$$\iint g_\sigma(x-\xi, y-\eta) g_\sigma(x-\xi', y-\eta') \sin(2\pi f x) \cos(2\pi f x) \,\mathrm{d}x \,\mathrm{d}y$$
$$= \frac{1}{2} \iint g_\sigma(x-\xi, y-\eta) g_\sigma(x-\xi', y-\eta') \sin(4\pi f x) \,\mathrm{d}x \,\mathrm{d}y$$
$$= \frac{1}{8\pi^2\sigma^4} e^{-\frac{(\xi-\xi')^2+(\eta-\eta')^2}{4\sigma^2}} \iint e^{-(x^2+y^2)/\sigma^2} \sin(4\pi f(x + \frac{\xi+\xi'}{2})) \,\mathrm{d}x \,\mathrm{d}y$$
$$= \frac{1}{8\pi^2\sigma^4} e^{-\frac{(\xi-\xi')^2+(\eta-\eta')^2}{4\sigma^2}} \pi\sigma^2 e^{-4\pi^2\sigma^2 f^2} \sin(2\pi f(\xi+\xi'))$$
$$= \frac{1}{8\pi\sigma^2} e^{-\frac{(\xi-\xi')^2+(\eta-\eta')^2}{4\sigma^2}} \sin(2\pi f(\xi+\xi')) e^{-4\pi^2\sigma^2 f^2}$$

by taking the imaginary part of eq. (127) from proposition B.1 and $\alpha = 2f$ and $\beta = f(\xi+\xi')$.
□

References

[1] P. Abrahamsen. A review of Gaussian random fields and correlation functions. Technical report, Norwegian Computing Center, Oslo, 1997.

[2] T.M. Atanackovic and A. Guran. *Theory of Elasticity for Scientists and Engineers*. Springer, 2000.

[3] F. Auger, E. Chassande-Mottin, and P. Flandrin. On phase-magnitude relationships in the short-time Fourier transform. *IEEE Signal Processing Letters*, 19(5):267–270, 2012.

[4] C. Badulescu, M. Bornert, J.-C. Dupré, S. Equis, M. Grédiac, J. Molimard, P. Picart, R. Rotinat, and V. Valle. Demodulation of spatial carrier images: performance analysis of several algorithms. *Experimental Mechanics*, 2012. Submitted.

[5] C. Badulescu, M. Grédiac, and J.-D. Mathias. Investigation of the grid method for accurate in-plane strain measurement. *Measurement Science and Technology*, 20(9):095102, 2009.

[6] C. Badulescu, M. Grédiac, J.-D. Mathias, and D. Roux. A procedure for accurate one-dimensional strain measurement using the grid method. *Experimental Mechanics*, 49:841–854, 2009.

[7] P. Balazs, D. Bayer, F. Jaillet, and P. Søndergaard. The phase derivative around zeros of the short-time Fourier transform. *ArXiv e-prints*, (1103.0409), March 2011.

[8] L. Cohen. *Time-frequency analysis*. Prentice-Hall, 1995.

[9] N. Delprat, B. Escudié, Ph. Guillemain, R. Kronland-Martinet, P. Tchamitchian, and B. Torrésani. Asymptotic wavelet and Gabor analysis: Extraction of instantaneous frequencies. *IEEE Transactions on Information Theory*, 38(2):644–664, 1992.

[10] J.-C. Dupré, F. Brémand, and A. Lagarde. Numerical spectral analysis of a grid: Application to strain measurements. *Optics and Lasers in Engineering*, 18(3):159–172, 1993.

[11] M. Grédiac, F. Sur, C. Badulescu, and J.-D. Mathias. Using deconvolution to improve the metrological performance of the grid method. Research Report 8127, INRIA, November 2012.

[12] E. Héripré, M. Dexet, J. Crépin, L. Gélébart, A. Roos, M. Bornert, and D. Caldemaison. Coupling between experimental measurements and polycrystal finite element calculations for micromechanical study of metallic materials. *International Journal of Plasticity*, 23(9):1512–1539, 2007.

[13] F. Jaillet, P. Balazs, M. Dörfler, and N. Engelputzeder. On the structure of the phase around the zeros of the short-time Fourier transform. In *Proceedings of NAG/DAGA International Conference on Acoustics*, pages 1584–1587, Rotterdam, Netherlands, 2009.

[14] Q. Kemao. Two-dimensional windowed Fourier transform for fringe pattern analysis: Principles, applications and implementations. *Optics and Lasers in Engineering*, 45(2):304–317, 2007.

[15] S. Mallat. *A wavelet tour of signal processing (2nd edition)*. Academic Press, 1999.

[16] R. D. Rajaona and P. Sulmont. A method of spectral analysis applied to periodic and pseudoperiodic signals. *Journal of computational Physics*, 61(1):186–193, 1985.

[17] Y. Surrel. *Photomechanics*, volume 77 of *Topics in Applied Physics*, chapter Fringe analysis, pages 55–102. Springer, 2000.

[18] M. Sutton, J.-J. Orteu, and H. Schreier. *Image Correlation for Shape, Motion and Deformation Measurements*. Springer, 2009.

[19] M. Takeda, H. Ina, and S. Kobayashi. Fourier-transform method of fringe-pattern analysis for computer-based topography and interferometry. *Journal of the Optical Society of America*, 72(1):156–160, 1982.

Contents

RESEARCH CENTRE
NANCY – GRAND EST

615 rue du Jardin Botanique
CS20101
54603 Villers-lès-Nancy Cedex

Publisher
Inria
Domaine de Voluceau - Rocquencourt
BP 105 - 78153 Le Chesnay Cedex
inria.fr

ISSN 0249-6399